


Unified limit-cycle amplitude prediction and symmetry-breaking analysis of combustion instabilities

V. Latour¹ , D. Durox¹, A. Renaud¹ and S. Candel¹

¹Laboratoire EM2C, CNRS, CentraleSupélec, Université Paris-Saclay, 3, rue Joliot Curie, 91192 Gif-sur-Yvette cedex, France

Corresponding author: V. Latour, veranika.latour@centralesupelec.fr

(Received 19 July 2024; revised 4 November 2024; accepted 24 December 2024)

Combustion instability analysis in annular systems often relies on reduced-order models that represent the complexity of combustion dynamics in a framework in which the flame is represented by a ‘flame describing function’ (FDF), portraying its heat release rate response to acoustic disturbances. However, in most cases, FDFs are only available for a limited range of disturbance amplitudes, complicating the description of the saturation process at high oscillation levels leading to the establishment of a limit cycle. This article shows that this difficulty may be overcome using a novel experimental scheme, relying on injector staging and in which the oscillation amplitude at limit cycle can be controlled, enabling us to measure FDFs from simultaneous pressure and heat release rate recordings. These data are then exploited to replace the standard modelling, in which the heat release rate is expressed as a third-order polynomial of pressure fluctuations, by a function of the modulation amplitude, allowing an easier adaptation to experimental data. The FDF is then used in a dynamical framework to analyse a set of staging configurations in an annular combustor, where two families of injectors are mixed and form different patterns. The limit-cycle amplitudes and the coupling modes observed experimentally are suitably retrieved. Finally, an expression for the growth rate is derived from the slow-flow variable equations defining the modal amplitudes and phase functions, which is shown to exactly agree with that obtained previously by using acoustic energy principles, providing a theoretical link between growth rates and limit-cycle amplitudes.

Key words: combustion, acoustics

1. Introduction

Research on thermoacoustic instabilities has led to significant advances in the understanding of the driving and coupling processes at stake. This effort, motivated by

practical issues, has been aimed in particular at developing reduced-order models and tools that allow the prediction of these undesired phenomena, enable the design of systems free of instabilities or help reduce the amplitude of oscillations if they occur. In recent years, research has been specifically directed at instabilities coupled by azimuthal modes in annular combustors, a geometry that is found in many aeroengines and gas turbines (O'Connor, Acharya & Lieuwen 2015; Poinso 2017; Schuller, Poinso & Candel 2020). To describe combustion systems' dynamics, one needs to characterize the flame response to acoustic disturbances. This response is usually represented by a flame transfer or describing function (FTF and FDF, respectively), which links, through a gain and a phase, the relative heat release rate (HRR) fluctuations to an input, that may be relative volume flow rate disturbances, relative equivalence ratio fluctuations or pressure fluctuations (Dowling 1997; Noiray *et al.* 2008; Schuller *et al.* 2020). The describing function concept is the nonlinear extension of the FTF and is used to capture the effects of the oscillation amplitude on the flame response. It can suitably describe the saturation process of the HRR fluctuations which takes place at high modulation amplitudes, reducing the flames' response and explaining why oscillations reach a limit cycle after a phase of growth (Dowling 1997; Lieuwen 2003; Balachandran *et al.* 2005; Noiray *et al.* 2008). Flame describing function measurements are available in the literature, but they are often limited to weakly nonlinear cases. Experiments and numerical simulations documenting the nonlinear flame response at high modulation amplitudes, close to those observed during limit-cycle oscillations (Wolf *et al.* 2012; Prieur *et al.* 2018), are less common, and this lack of knowledge has been replaced by a modelling of the nonlinear behaviour of the HRR fluctuations at high modulation amplitudes to allow an examination of the evolution to limit cycles.

In the present article, we use recent experiments (Alhaffar *et al.* 2024) in the annular combustor MICCA-Spray, which will be designated from here on as MICCA, to propose an alternative representation of the HRR fluctuations in terms of the pressure oscillation amplitude. This new formulation is employed in a generic problem to analyse the evolution to limit cycle using slow-flow variable equations. This study then builds upon the modelling framework proposed by Ghirardo, Juniper & Moeck (2016), which, in combination with the recent flame response measurements obtained in MICCA, is applied to predict the limit-cycle oscillation amplitudes for a set of staging configurations investigated in Latour *et al.* (2024a). Exploiting the large experimental dataset collected in MICCA together with dynamical equations, this work aims to address the following issues:

- (i) Can one define an alternative representation of the HRR nonlinearity as a function of the level of oscillation that is more flexible and more easily adaptable to experimental flame dynamics data than current models?
- (ii) Using the slow variable equations in combination with the new representation of the flame response, is it possible to predict the various limit-cycle amplitudes for the different staging configurations and retrieve the experimental trends and data?
- (iii) Finally, can one derive an expression for the growth rate from the slow-flow variables' dynamical equations and does this expression match with another previously obtained from acoustic energy balance principles (Latour *et al.* 2024a)?

At this point, it is natural to review the literature, but for brevity, we only consider investigations dealing with the modelling of HRR fluctuations in terms of pressure fluctuations and that are specifically aimed at analysing the behaviour of annular combustors. In a seminal investigation, Noiray, Bothien & Schuermans (2011) propose

an expression for the HRR fluctuations, \dot{Q}' , in the form of a third-order polynomial of the pressure disturbances p : $\dot{Q}'(p) = \beta p - \kappa p^3$, with β and κ , the linear and saturation coefficients, respectively. When this expression is injected in the wave equation representing the system dynamics and the pressure field is projected on the normal modes, it is found that the modal amplitudes satisfy second-order differential equations that behave like coupled Van der Pol oscillators and feature a finite amplitude limit cycle. This is then used to analyse various issues, like the nature of the coupling mode and symmetry breaking. One difficulty with this kind of modelling is that the polynomial expression matches experimental data when the amplitudes of oscillation are small, but diverges from the measurements when the amplitude takes large values, as indicated in the same article, by making use of data from Balachandran *et al.* (2005). This difficulty was also pointed out by Prieur *et al.* (2018), using signals from strong instability bursts in an annular combustor, where the relation between the relative HRR and the pressure amplitude was found to be quasi-linear. Using the same flame response model but introducing a stochastic forcing term, Noiray & Schuermans (2013) were then able to account for turbulence effects, inherent to high-power combustors, and in particular for the switching between spinning and standing modes observed in experiments and numerical simulations, which could not be retrieved with a purely deterministic approach. Another extension of this model by Ghirardo & Juniper (2013) was meant to account for the HRR dependence on the azimuthal velocity, v'_θ , acting on the flame in the transverse direction. Using $\dot{Q}'(p, v'_\theta) = (\beta p - \kappa p^3)\mu(v'_\theta)$, where μ is a function of the azimuthal velocity, it was shown that stable standing mode solutions existed in rotationally symmetric annular configurations. Effects of a time lag were investigated at a later stage by Ghirardo, Juniper & Bothien (2018), by writing the HRR as a third-order polynomial of the pressure delayed by a time lag τ , $p(t - \tau)$. It was shown that large delays corresponding to steep phase changes with respect to frequency promoted the occurrence of instabilities. This was complemented by Bonciolini *et al.* (2021), who considered effects of random turbulence-induced perturbations of the flame phase.

Although much of the work, including the present study, consider oscillations associated with two degenerate modes, there are cases where the coupling involves multiple modes (Moeck & Paschereit 2012). This was exemplified in Moeck *et al.* (2019) where two degenerate azimuthal modes and an axial mode were included together with the third-order polynomial expression of the HRR to explain the ‘slanted mode’ observed in the annular configuration MICCA equipped with matrix injectors. Results indicated that synchronized oscillations were generic features of annular combustors. This analysis was pursued by Orchini & Moeck (2024) in the case of can-annular combustors by representing this geometry by N coupled oscillators to identify conditions leading to mode locking at a common frequency. Here too, the HRR model relied on a third-order polynomial $\dot{q}'_j(x, t) = [\beta p(x, t) - \kappa p(x, t)^3]\delta(x_{fj})$, where $\delta(x_{fj})$ is the Dirac function representing the j th flame as a point source.

The investigation of thermoacoustic systems can be carried out in the time domain or frequency domain. Most time domain studies use the cubic polynomial formulation for the HRR. Kashinath, Waugh & Juniper (2014) proposed an alternative approach where the flame is modelled using the G -equation, but this solution is difficult to extend to turbulent flames. In the frequency domain, the HRR operator is commonly represented in the form of a FDF, characterizing the flame response to an input signal at a given frequency and amplitude. This was exemplified in the pioneering nonlinear analysis of an unstable ducted flame by Dowling (1997). The application of the FDF to the prediction of limit-cycle amplitude, mode switching, instability triggering and frequency shifting during growth to the limit cycle was demonstrated by Noiray *et al.* (2008). The FDF

concept is now widely used in reduced-order combustor models to derive dispersion relations $\mathcal{D}(\omega, a) = 0$ depending on frequency and amplitude and giving access to the evolution of the growth rate with the oscillation level, $\omega_i = \omega_i(a)$ (Paliès *et al.* 2011; Schuller *et al.* 2020; Rajendram Soundararajan *et al.* 2022a). These investigations often rely on an acoustic network of the combustor or a Helmholtz solver if the geometry is complex, as in Laera *et al.* (2017), to determine the system trajectory in the frequency-growth rate plane as a function of the oscillation amplitude. The use of measured FDFs combined with a reduced-order acoustic network model exploited by Orchini, Mensah & Moeck (2019) allowed them, for example, to retrieve experimental data from MICCA. However, approaches based on FDFs are only valid if the system oscillations are dominated by a single frequency (Stow & Dowling 2009). To deal with non-periodic oscillation cases, the concept of the ‘flame double input describing function’ was, for example, introduced by Orchini & Juniper (2016), where the flame response is sought for a forcing signal composed of two amplitudes and two frequencies. Higher harmonics can also be included in the FDF formulation (see Haeringer, Merk & Polifke 2019). When the flame nonlinearity is expressed in the time domain, it is interesting to link it to a frequency domain representation, a point discussed by Ghirardo *et al.* (2015) and Ghirardo *et al.* (2018). Conversely, Stow & Dowling (2009) give an example of how a describing function can be translated in the time domain for thermoacoustic investigations.

On the experimental level, much effort has been made to determine describing functions in the frequency domain, usually in single-sector configurations (Rajendram Soundararajan *et al.* 2022b; Schuller *et al.* 2022; Wiseman, Gruber & Dawson 2023). However, some recent studies carried out by Nygård *et al.* (2019) and Nygård, Ghirardo & Worth (2021) under external modulation in an annular combustor indicate that the HRR response of the flames to azimuthal waves spinning in clockwise (CW) or counterclockwise (CCW) directions may be different, leading Nygård, Ghirardo & Worth (2023) to derive a multiple input single output flame response model in which the HRR depends on the ‘nature’ angle χ , that represents the relative amplitudes of CW and CCW waves in the quaternion framework. In this azimuthal FDF framework, the nature angle of the acoustic mode and that of the HRR distribution may not be the same.

The description of azimuthal pressure fields and their evolution in time generally relies on two kinds of formulations, the first using the quaternion concept (Ghirardo & Bothien 2018) in which the slow-flow variables are the amplitude A , the nature angle χ , the orientation angle θ_0 and a phase φ . The second option is based on state variables comprising the amplitudes A_1 and A_2 and the phases φ_1 and φ_2 of the two waves composing the field in the system. The quaternion variables were exploited, for example, by Faure-Beaulieu & Noiray (2020), Faure-Beaulieu *et al.* (2021), Indlekofer *et al.* (2022) and Faure-Beaulieu, Pedernana & Noiray (2023) to examine the nature of the unstable oscillations or symmetry breaking induced by asymmetries in the HRR distribution and by the mean swirl flow. The second option employed, for example, by Ghirardo *et al.* (2016) and Ghirardo, Boudy & Bothien (2018), together with a flame response in the form of an operator depending on the local pressure, enabled the authors to obtain dynamical equations derived for the slow-flow amplitude and phase variables, which were used to investigate the stability of standing and spinning solutions and, by perturbing the flame responses, Ghirardo *et al.* (2021) examined symmetry-breaking effects. However, to the authors’ knowledge, this framework has not been used to analyse injector staging experiments of the kind reported in the present article.

The goal of the present investigation is to revisit the question of flame modelling in light of recent experiments in which the flames’ HRR response to pressure fluctuations is experimentally determined in the MICCA annular set-up for a wide range of limit-cycle

oscillation levels (Alhaffar *et al.* 2024). The limit-cycle amplitude is controlled by making use of various injector arrangements, mixing two kinds of units designated as ‘U’ and ‘S’ (Latour *et al.* 2024a). Experiments indicate that, when the annular combustor is equipped with U-injectors, the regimes of operation may be stable or unstable. In contrast, when the system is equipped with S-injectors, it only features stable regimes (Rajendram Soundararajan *et al.* 2022b). Mixing the two types of injectors enables a standing mode with a controlled nodal line position to be favoured and gives access to limit cycles with a wide range of amplitude levels. The data gathered are used to determine pressure-based FDFs, linking the flames’ HRR response to pressure disturbances. This FDF is then used as an input in a dynamical model of the type proposed by Ghirardo *et al.* (2016) to calculate the limit cycles corresponding to the different staging patterns tested in MICCA. The slow-flow variable equations then enable us to examine the evolution towards the limit cycle, discuss the modal nature corresponding to different staging patterns and compare results of calculations with experimental data. An expression for the growth rate is finally derived from the slow variables’ dynamical equations and compared with that deduced from acoustic energy balance principles by Latour *et al.* (2024a).

This article begins with a brief description of the MICCA experimental set-up (§ 2). The pressure-based FDFs measured for the flames formed by injectors U and S are discussed in § 3 and a model linking the flames’ HRR response to the amplitude of pressure disturbances is proposed. Two HRR formulations and their impact on the dynamics of slow-flow variables are then examined in § 4 by considering a generic problem in which the system features a single non-degenerate mode. This is used as a testbed to analyse different nonlinear expressions of the HRR in the simplest possible situation. The experimentally determined pressure-based FDFs are next used as an input in a dynamical model in § 5, and the model’s limit-cycle amplitudes and nature predictions are compared with the experimental observations for various staging patterns in MICCA. It is finally shown, in § 6, that the growth rate extracted from the slow-flow variable differential equations yields an expression that can be compared with that previously derived from acoustic energy considerations. Systematic calculations relying on the slow-flow variable equations and the growth rate expression are then used to pursue the comparison between predictions and experimental data for the whole set of staging patterns tested in MICCA.

2. Experimental configuration and modal identification

2.1. *The MICCA annular combustor and injectors’ characteristics*

The laboratory-scale annular combustor MICCA, shown in [figure 1\(a\)](#), is used to investigate thermoacoustic instabilities coupled by azimuthal modes. The combustion chamber is formed by two cylindrical quartz walls of height $l = 400$ mm, of outer diameter 300 mm for the inner quartz and inner diameter 400 mm for the outer quartz. The backplane comprises 16 regularly spaced injection units delivering liquid heptane in the form of a hollow cone spray of droplets. The air flow rate is controlled with two Bronkhorst EL-FLOW flow meters and the fuel flow rate with a Bronkhorst CORI-FLOW controller. Eight Brüel & Kjær microphones are mounted on waveguides and plugged on the chamber backplane to record the pressure fluctuations at a sampling rate $f_s = 32\,768$ Hz. An array of 8 photomultipliers equipped with an OH* filter centred at 310 nm records the light emitted by eight adjacent flames (see [figure 1\(b\)](#)). A mask is placed in front of each flame to ensure that each PM only records the light emitted by one flame. A cylindrical mask is also placed inside the inner cylindrical quartz to hide the flames in the background, as can be seen in [figure 1\(c\)](#), showing the MICCA combustor under operation.

Injector	S_N	Δp (kPa)	σ
Injector S (stable in MICCA-spray)	0.60	3.65	3.33
Injector U (unstable in MICCA-spray)	0.74	5.70	5.20

Table 1. Injectors' characteristics: swirl number (S_N), pressure drop (Δp) and pressure drop coefficient (σ), obtained from measurements under cold flow conditions for an air mass flow rate of 2.3 g s^{-1} (Vignat *et al.* 2021).

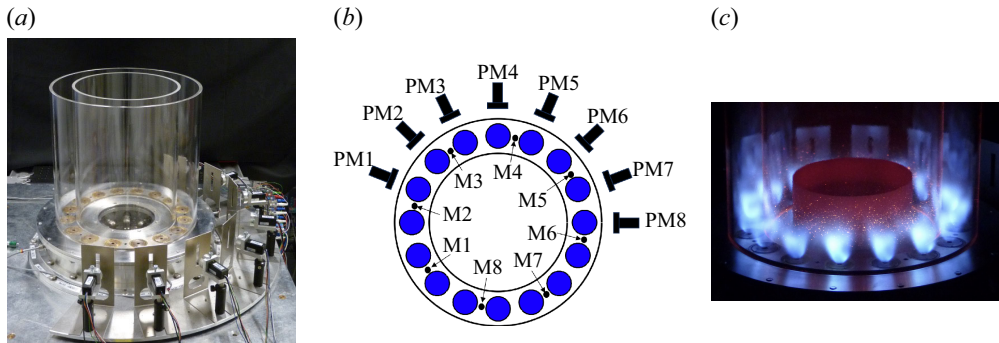


Figure 1. (a) The MICCA annular combustor with an array of eight photomultipliers. (b) Microphones (labelled 'MX') and photomultiplier positions (labelled 'PMX'). (c) View of the MICCA combustor under operation.

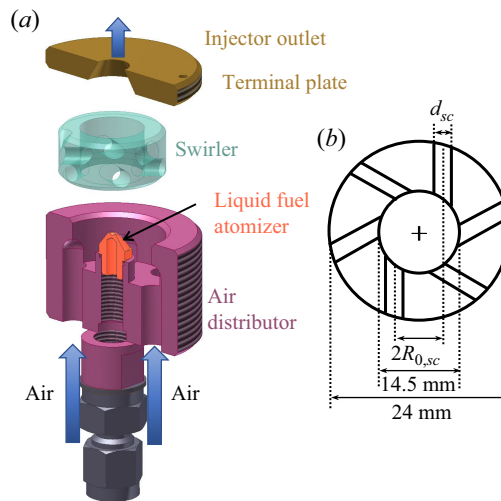


Figure 2. Exploded view of an injection unit, showing its main components (a). A top view of the swirler appears in (b).

The injectors, for which an exploded view is presented in figure 2(a), comprise four main elements: an air distributor, an atomizer, a swirler and a terminal plate. Changing the swirler (tangential channels' radius and orientation figure 2b) modifies the pressure drop and the swirl number of the units. Two types of injectors are used in this work: a low-swirl low-pressure drop and a high-swirl high-pressure drop, designated respectively as

‘injector S’ and ‘injector U’. The characteristics of the two injectors are gathered in table 1. Additional information on the dynamics of the flames formed by these two injectors is given by Rajendram Soundararajan *et al.* (2022b) and Latour *et al.* (2024a).

In the present study, the annular combustor is operated at a thermal power $\mathcal{P} = 118$ kW and a global equivalence ratio $\phi = 0.9$. Under these operating conditions, MICCA is stable when equipped with S-injectors and unstable when 16 U-injectors are mounted on the backplane.

2.2. Modal structure and oscillation frequency

An acoustic analysis of the MICCA combustor has to be carried out to identify the eigenmodes susceptible to being involved in the combustion/acoustics coupling. As discussed in Latour *et al.* (2024a), the combustion chamber in MICCA is decoupled from the plenum by the injectors that are weakly transparent to acoustic waves and introduce an important area change between the chamber and the plenum. The coupling of the injector ports’ acoustics with the combustion chamber acoustics can also be neglected, as shown in the acoustic analysis of MICCA presented in the supplementary material available at <https://doi.org/10.1017/jfm.2025.10>. One can hence assume that the modes that need to be considered are those of the chamber, where the backplane can be assimilated to a rigid wall and the outlet can be modelled as being open to the atmosphere. Experiments indicate that the first azimuthal–first longitudinal (1A1L) mode is involved in the combustion/acoustics coupling in MICCA (Latour *et al.* 2024a). Neglecting the radial dependence, the pressure field can then be cast in the form

$$p(x, \theta, t)_{1A1L} = [A_+ \exp(i\theta - i\omega t + i\phi_+) + A_- \exp(-i\theta - i\omega t + i\phi_-)]\psi_{1L}(x), \quad (2.1)$$

where $A_+ \exp(i\phi_+)$ and $A_- \exp(i\phi_-)$ correspond to the complex amplitudes of the CCW and CW spinning waves respectively, θ designates the azimuthal coordinate considered positive in the CCW direction and ω is the angular frequency. In the previous expression, $\psi_{1L}(x) = \cos[\pi x/(2l')]$ is the axial wave function satisfying the boundary conditions on the chamber backplane and at its exhaust, with $l' = l + \delta_a$, l being the chamber length and δ_a the end correction. For MICCA, pressure measurements near the chamber exhaust indicate that $\delta_a \simeq 0.044$ m so that $l' \simeq 0.44$ m (Laera *et al.* 2017).

The eigenfrequency corresponding to the 1A1L mode is

$$f_{1A1L} = \left[\left(\frac{c}{\mathcal{P}_a} \right)^2 + \left(\frac{c}{4l'} \right)^2 \right]^{1/2}, \quad (2.2)$$

where $\mathcal{P}_a = 2\pi R$ is the mean perimeter of the system and c the speed of sound. In the MICCA experiments, the perimeter is $\mathcal{P}_a \simeq 1.1$ m. Assuming an average temperature in the chamber of $T \simeq 1400$ K (estimated from exhaust gas temperature measurements carried out by Vignat (2020) with a thermocouple in the single-sector counterpart of the MICCA annular set-up), defining a speed of sound $c = 754$ m s⁻¹, the eigenfrequency of the 1A1L mode is $f_{1A1L} \simeq 808$ Hz.

The complex wave amplitudes $A_+ \exp(i\phi_+)$ and $A_- \exp(i\phi_-)$ may be retrieved from the eight microphone signals by solving an over-determined system of linear equations using a least squares algorithm. One may then deduce the instability amplitude, defined as

$$A = [A_+^2 + A_-^2]^{1/2}. \quad (2.3)$$

It is worth noting that A is equal to the quaternion formulation amplitude divided by $\sqrt{2}$. Finally, the frequency of the instability, f , is experimentally determined from the power spectral density of the pressure signals, calculated using Welch’s method applied to 63

blocks of 8192 samples and a Hamming window weighting with a 50 % overlap. The frequency resolution for these conditions is $\Delta f = 4$ Hz.

At this point it is worth recalling that the frequency of oscillation of a thermoacoustic system ('closed-loop' case) is close to the eigenfrequency of the mode (the 'open-loop' frequency) but does not coincide with it because of the shift introduced by the presence of the flames. This shift depends on the flame dynamical characteristics (FDF) and on the set of parameters that also govern the growth rate (Schuller *et al.* 2020). One may show (see Schuller *et al.* 2020 or § 4) that the relative frequency shift, $\Delta\omega/\omega_0$, is linked to the growth rate, ω_i , by $\Delta\omega/\omega_0 \simeq -(\omega_i/\omega_0) \tan \varphi_p$, where φ_p represents the phase between the pressure and the HRR signals. Since $\omega_i/\omega_0 < 1$ and $\varphi_p \simeq 0$ in an unstable situation, one deduces that $|\Delta\omega/\omega_0| \ll 1$. The previous argument indicates why the shift in frequency is in most cases below 5 % of the modal eigenfrequency, as can be seen in the data compiled by Ghirardo *et al.* (2018) or in figures showing the evolution of thermoacoustic systems in the frequency/growth rate plane reported by Noiray *et al.* (2008), Paliès *et al.* (2011) and Laera *et al.* (2017) and confirmed by experimental results obtained in MICCA (Rajendram Soundararajan *et al.* 2022b; Latour *et al.* 2024a).

As pointed out by one reviewer, other aspects of the system, like the temperature distribution linked to the presence of the flames, may also intervene, and affect the modal structure of the azimuthal mode, a phenomenon not accounted for in (2.2), used to determine the frequency of the 1AIL mode of the combustion chamber in MICCA. The temperature distribution can, for example, be easily taken into account by making use of a Helmholtz solver to obtain the modal distributions and eigenfrequencies, as done in previous works (Bourgouin *et al.* 2013; Laera *et al.* 2017). It was found that the obtained eigenfrequencies were not very different from those calculated using theoretical expressions if the mean speed of sound c , and hence the temperature in the combustion chamber, are suitably determined, for example, from exhaust gas temperature measurements, as proposed in this work from results reported by Vignat (2020). The shift in frequency being estimated to be less than a few per cent of the open-loop frequency (obtained from self-sustained oscillation measurements in MICCA), and the calculated value of the open-loop frequency (808 Hz) from the burnt gas temperature estimate falling in the range of frequencies corresponding to observed oscillations (around 800 Hz), one can have confidence in the estimated value. It is, however, interesting to determine the effect of an error in the estimation of the temperature on the calculated frequency of oscillation. To that end, one may consider, for instance, an error $\Delta T = 100$ K. The variation in modal frequency is then given by $\Delta f/f \simeq \Delta c/c = (1/2)\Delta T/T$. Taking $T = 1400$ K, one finds that $\Delta f/f \simeq 3.5$ % and for a frequency $f = 800$ Hz this would induce a variation $\Delta f \simeq 28$ Hz.

3. Pressure-based FDF measurements in MICCA

MICCA is now used to collect experimental data on the flames' HRR responses to pressure oscillations of various amplitudes, which will be presented in the form of a describing function, expressed in the frequency domain. Mixing U- and S-injectors enables us to control the level of limit-cycle pressure fluctuations and favour a standing mode with a fixed nodal line position, as described in Latour *et al.* (2024a). Simultaneous pressure and photomultiplier recordings at different flame positions with respect to the nodal line location may then be used to determine a 'pressure-based FDF' (Alhaffar *et al.* 2024), defined as

$$\mathcal{F}_p(f, \Pi_j) = \frac{\widehat{Q}_j/\overline{Q}}{\widehat{p}_j/\rho U_b^2} = G_p(f, \Pi_j)e^{i\varphi(f, \Pi_j)}, \quad (3.1)$$

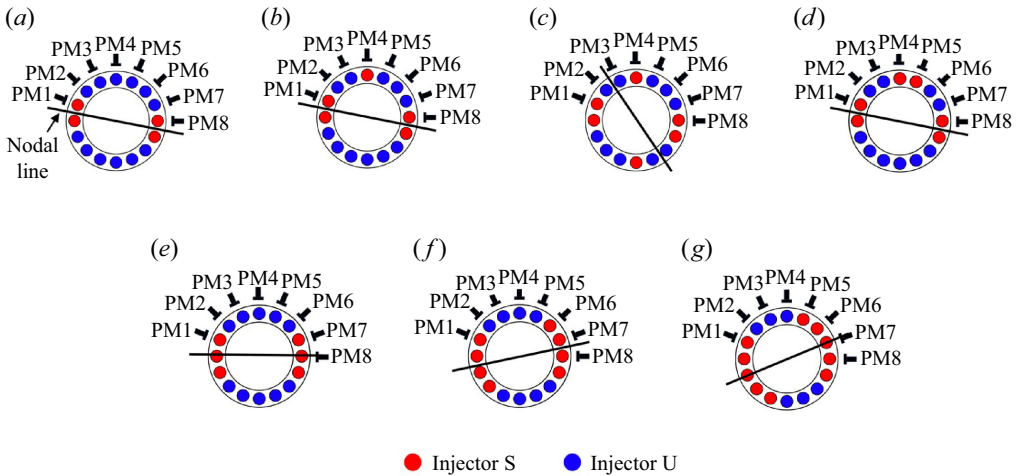


Figure 3. Staging configurations used for pressure-based FDF measurements showing the placement of the injectors U and S and the photomultiplier positions. The nodal lines observed experimentally are represented by black solid lines.

where the index j designates the flame number, f the frequency, \hat{Q}_j/\bar{Q} the relative HRR fluctuations and $\hat{p}_j/\rho U_b^2$ the dimensionless pressure fluctuations. The reduced amplitude of the pressure fluctuations at the position of the j th flame is defined by $\Pi_j = (p_{rms})_j/(\rho U_b^2)$, with ρ the density, taken at the fresh gas temperature, and U_b the bulk velocity at the injector outlet, equal to 46 m s^{-1} for the investigated operating conditions. It is worth mentioning that the pressure-based FDF defined in this way may be linked to the velocity-based FDF, commonly determined in thermoacoustic investigations (see, for example, Noiray *et al.* 2008), through an effective impedance, as discussed in Appendix A.

Seven staging patterns, shown in figure 3, are used for the pressure-based FDF measurements. These injector configurations were selected because they lead to a well-defined standing mode with a controlled nodal line position (Latour *et al.* 2024a,b) and pressure fluctuation levels enabling a good signal-to-noise ratio for the pressure and photomultiplier recordings. The self-sustained oscillation amplitudes obtained in this way vary between 300 and 1400 Pa, and the instability frequencies lie in the [774, 802] Hz range. Additional information on the determination of pressure-based FDFs can be found in Alhaffar *et al.* (2024), together with a comparison with data from experiments on a linear array of injectors modulated in the transverse direction.

At this point, it is important to stress that, contrary to an externally forced situation, the procedure used in this work to collect the pressure-based FDF data relies on the ability to obtain self-sustained oscillations in MICCA with a well-defined standing mode. The modulation frequency defining flame oscillations in each staging configuration hence results from the closed-loop interaction between the acoustics of the MICCA combustor and the flames, and is therefore dependent on the staging pattern. As discussed in Alhaffar *et al.* (2024), the self-sustained oscillation frequencies of the seven staging patterns used for pressure-based FDF determination vary between 774 and 802 Hz. Although this range of frequency variation is limited, one needs to check that these changes in self-sustained oscillation frequencies do not lead to differences in the flame response. This is done in the supplementary material, where the FDF data points are coloured by the frequency value. There is no visible trend with respect to the relatively small frequency variations and one

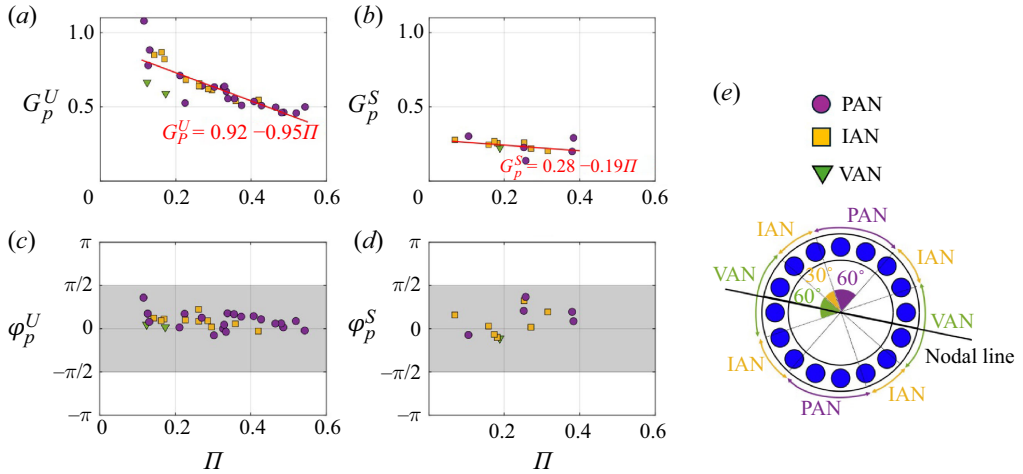


Figure 4. Pressure-based FDF gain (a,b) and phase (c,d) as a function of Π for injectors U (a,c) and S (b,d). The colours correspond to the ‘PAN’, ‘IAN’ and ‘VAN’ regions, as defined in (e).

may conclude that the frequency differences between the staging patterns do not affect the collected pressure-based data.

As also pointed out by a reviewer, flame dynamics data are usually presented as a function of the frequency but this is not the case here. Indeed, in the modelling framework adopted in this work, it is admitted that the frequency of interest is that of the eigenmode involved in the combustion/acoustic coupling and that only the dynamics around the 1AIL eigenfrequency is of interest. This is why flame dynamics data are presented at this frequency only, as in the other investigations of this kind (Ghirardo *et al.* 2016, 2018, 2021).

The pressure-based FDF gains and phases are plotted as a function of the reduced amplitude of pressure fluctuations, Π , in figure 4 for injectors U (figure 4a,c) and S (figure 4b,d). For the interpretation of the results, the points are labelled ‘PAN’ (pressure anti-node), ‘IAN’ (intensity anti-node) and ‘VAN’ (velocity anti-node), depending on their position with respect to the nodal line location, as defined in Alhaffar *et al.* (2024) and shown in figure 4(e). The data obtained for flames established at various positions with respect to the nodal line indicate that the flame location does not significantly influence its response. The corresponding FDF data points follow nearly similar trends and may be treated independently of their position with respect to the nodal line. The gain values for injector U are higher than those pertaining to injector S, while the phases are close to 0 for the two injectors. For both injectors, the decrease in the gain of the pressure-based FDF with the local pressure amplitude Π , corresponding to flame saturation, follows a nearly linear trend of the form: $G_p = \beta - \kappa\Pi$. At this point, it is worth noting that β and κ defining the linear and saturation coefficients are dimensionless quantities which differ from the dimensional coefficients used in the cubic formulation of Noiray *et al.* (2011). The coefficients β and κ , that are here deduced from a least squares regression for the two injectors U and S, define the linear models superimposed on the data points in figure 4.

As indicated by a reviewer, other expressions, such as higher-order polynomial functions, could be used to fit the experimental FDF data. It is found, however, that the R^2 statistical index is only slightly improved when using second-order or cubic polynomials as it changes from 0.69 to 0.74 for injector U. However, by using higher-order fits (cubic or fourth-order polynomials), one runs the risk of over-fitting, and some points, which appear

like ‘outliers’, may weigh in the fit although they should not. This is why the linear fit is a good compromise in terms of data representation and ease of insertion in an analytical formulation. This is confirmed in the sensitivity analysis carried out in § 5.6 for the linear and quadratic fits where one examines effects of errors in the fitting on the predicted limit-cycle oscillation amplitudes.

To finish, the relatively large dispersion in the FDF gain and phase values observed for injector S is due to a higher uncertainty in the measurements, since S-injectors are mainly located close to the pressure nodal line where pressure fluctuations are low. This might also be linked to differences between injectors, as reported by Nygård, Ghirardo & Worth (2021), where different responses were observed for flames submitted to a spinning mode and interpreted as resulting from small symmetry-breaking effects.

4. Investigation of two heat release rate formulations

Before using the pressure-based FDFs obtained in § 3 in an analytical framework (§ 5), two HRR formulations are examined in a simplified framework to investigate the impact of the flame response model on the slow-flow variables’ dynamics: the first is the cubic polynomial formulation, introduced by Noiray *et al.* (2011), $\dot{Q}' = \beta^* p - \kappa_1^* p^3$, and the second is of the form $\dot{Q}' = g^*(a)p$, where the saturation process is a function g^* of the slowly varying instability amplitude a of the form $g^*(a) = \beta^* - \kappa_2^* a$, as observed in the experimental data reported in § 3. In the two models investigated, the saturation coefficients will be denoted κ_1^* and κ_2^* , and since they intervene in different formulations, their dimensions and values are also different.

For simplicity, a single oscillator model is considered in this section. Physically, this situation corresponds, for example, to a thermoacoustic system with a self-sustained longitudinal oscillation. The case of azimuthal modes in an annular system will be considered in § 5.

4.1. Polynomial heat release rate fluctuation formulation: $\dot{Q}' = \beta^* p - \kappa_1^* p^3$

The starting point is the non-homogeneous wave equation, derived from the combination of the mass, momentum and energy equations for low-Mach flows and perfect gases, to which a damping term is added in the form $\alpha(\partial p/\partial t)$ to account for the losses in the system

$$\frac{\partial^2 p}{\partial t^2} - \rho c^2 \nabla \cdot \frac{1}{\rho} \nabla p = (\gamma - 1) \frac{\partial \dot{q}'}{\partial t} - \alpha \frac{\partial p}{\partial t}. \quad (4.1)$$

In this expression, \dot{q}' , ρ , c and γ respectively designate the volumetric HRR fluctuations, the mean density, the mean speed of sound and the specific heat ratio. The steps leading to the derivation of (4.1) are recalled, for instance, in Nicoud *et al.* (2007, 2011) or Ghirardo *et al.* (2018).

At this stage, it is interesting to discuss the zero-Mach-number assumption used to write (4.1), which is common to most thermoacoustic investigations of annular systems (Nicoud *et al.* 2007, 2011; Ghirardo *et al.* 2016). In annular combustors that are typically used in gas turbines, the Mach number is low to ensure that the residence time of reactants is sufficient for flame stabilization, to allow complete conversion into products and minimize pressure losses associated with heat addition. The analysis by Nicoud *et al.* (2007) indicates that the mean flow terms can be neglected if the characteristic Mach number is small compared with the ratio of the flame dimension to the typical acoustic wavelength and this condition is generally fulfilled. There are, however, some more subtle

effects of the presence of a mean swirling flow on the acoustic modes in an annular system. If, for example, the azimuthal velocity is high enough, the global rotation of the flow will suppress the degeneracy of the azimuthal modes and the CW and CCW modes will feature different eigenfrequencies and growth rates (Bauerheim, Cazalens & Poinso 2015). It is also indicated by Faure-Beaulieu *et al.* (2023) that, when a swirl is imposed in a certain direction, a statistical preference is observed toward mixed states propagating against the swirl. However, in the situation at hand, the global rotation velocity is so small that the two eigenfrequencies cannot be distinguished in the spectral analysis of the microphone signals and the statistical preference is expected to be small compared with the symmetry-breaking effects induced by injector staging of the kind investigated in the present work.

A second assumption made in writing (4.1) is that the acoustics may be treated as a linear process. This is also widely adopted because the levels of relative pressure fluctuations in typical gas turbine combustion systems remain below a few per cent of the chamber pressure, in contrast with rocket thrust chambers where relative fluctuation levels may reach up to 40 % of the chamber pressure. The reader can find further details on the nonlinear acoustics in rocket engines in Culick (1994). In the case of gas turbines, the level of oscillation does not exceed a few per cent. In the MICCA experimental set-up, even at a pressure fluctuations level of 5000 Pa (5 % of the chamber pressure), the microphone signals remain sinusoidal while the light intensity signal from OH* radicals detected by photomultipliers facing the flames become highly nonlinear (Prieur *et al.* 2018). One may then safely assume that the acoustics is linear and that the main source of nonlinearity in the system is linked to the unsteady HRRs and that this nonlinearity can be represented with a FDF (Dowling 1997; Noiray *et al.* 2008).

Finally, it is also worth noting that the α appearing in this expression corresponds to the damping rate of acoustic energy and is equal to twice the damping rate of pressure. The value of this damping rate can be obtained in various ways using, for instance, system identification methods, as proposed in Boujo *et al.* (2016). Another possibility, used in this study (see § 5), relies on source term measurements at the limit cycle, as exemplified in Durox *et al.* (2009) or Latour *et al.* (2024b), which will be discussed, along with the modelling hypothesis, in § 5.

In flames that are nearly isobaric, the product ρc^2 is nearly constant and may be introduced in the divergence operator in (4.1). One may also assume that the flame is compact with respect to the acoustic wavelength and consider that the HRR fluctuations are concentrated at one point, \mathbf{x}_f . One may then write $\dot{q}' = \delta(\mathbf{x} - \mathbf{x}_f)\dot{Q}'$, where δ is the Dirac function and \dot{Q}' corresponds to the HRR fluctuations integrated over the volume of the flame. Hence, the wave equation may now be replaced by

$$\frac{\partial^2 p}{\partial t^2} - \nabla \cdot c^2 \nabla p = (\gamma - 1)\delta(\mathbf{x} - \mathbf{x}_f)\frac{\partial \dot{Q}'}{\partial t} - \alpha \frac{\partial p}{\partial t}. \quad (4.2)$$

The normal modes of this equation, in the absence of heat release and damping, are such that

$$\nabla \cdot c^2 \nabla \psi_n + \omega_n^2 \psi_n = 0, \quad (4.3)$$

where ω_n and ψ_n represent the modal eigenvalues and eigenfunctions, respectively. The pressure field can then be expanded on the orthogonal basis formed by the eigenmodes ψ_n , solutions of the homogeneous wave equation

$$p = \sum_n \eta_n(t) \psi_n(\mathbf{x}), \quad (4.4)$$

where η_n represents the amplitude of the n th mode. For homogeneous boundary conditions, the normal modes ψ_n are orthogonal (see for example Nicoud *et al.* 2007) and one may write

$$\int_V \psi_n \psi_m dV = \Lambda_n \delta_{mn} \text{ with } \delta_{nn} = 1 \text{ and } \delta_{mn} = 0 \text{ when } m \neq n. \quad (4.5)$$

Introducing the modal expansion (4.4) in the wave equation (4.2) and projecting the result on the normal modes, one obtains a set of differential equations for the modal amplitudes $\eta_n(t)$

$$\ddot{\eta}_n + \alpha \dot{\eta}_n + \omega_n^2 \eta_n = \frac{\gamma - 1}{\Lambda_n} \frac{\partial \dot{Q}'}{\partial t} \psi_n(x_f) \text{ for } n = 1, 2, \dots \quad (4.6)$$

For the sake of simplicity, it will be assumed in what follows that a single mode, characterized by an eigenfrequency ω_0 and a modal amplitude η , is involved in the combustion/acoustics coupling. This situation physically corresponds, for instance, to a coupling by a longitudinal mode in a single-injector set-up. This assumption is made to analyse the effects of the HRR formulation in the simplest possible framework. In this case, the pressure field reads

$$p = \eta(t) \psi(x). \quad (4.7)$$

One possibility, introduced by Noiray *et al.* (2011), consists in writing \dot{Q}' in the form of a third-order polynomial of the pressure $\dot{Q}' = \beta^* p - \kappa^* p^3$, which, using (4.7), reads

$$\dot{Q}' = \beta^* \eta \psi_f - \kappa_1^* \eta^3 \psi_f^3, \quad (4.8)$$

where $\psi_f = \psi(x_f)$. It is then convenient to define

$$\beta = [(\gamma - 1)/\Lambda] \beta^* \psi_f^2 \quad \text{and} \quad \kappa_1 = [(\gamma - 1)/\Lambda] \kappa_1^* \psi_f^4. \quad (4.9)$$

With these notations, the dynamical equation governing η becomes

$$\ddot{\eta} + \alpha \dot{\eta} + \omega_0^2 \eta = \beta \dot{\eta} - 3\kappa_1 \eta^2 \dot{\eta}. \quad (4.10)$$

In this expression, β is the linear rate of growth corresponding to small pressure perturbations and κ_1 is positive and governs the saturation process taking place at large oscillation amplitudes. The damping coefficient α is the rate at which η^2 decays as a function of time when the right-hand side of (4.10) is equal to zero.

Solutions of this nonlinear differential equation may be obtained by making use of the method of averaging introduced by Krylov & Bogoliubov (1950). This standard method is used here, as in most previous studies on azimuthal combustion instabilities referenced in the introduction. As pointed out by a reviewer, this method may not always yield the best approximation of the slow-flow variables, and other approaches, such as the multiple time scales method, can be used, as exemplified in Sirignano & Krieg (2016). The reader is also referred to Cole (1968), Nayfeh & Mook (1979) and Verhulst (1996) for additional information and the comparison of different approaches for the obtention of slow-flow variable equations. However, the advantage of the averaging method is that it gives access to the slow-flow variables with a reasonable amount of calculations and is sufficient to reveal the effects of the different HRR formulations.

The averaging method is quite standard, but the main steps are nevertheless provided here to facilitate the understanding of the derivation. The solution is first written in terms of a slowly varying amplitude a and a phase φ

$$\eta(t) = a(t) \cos[\omega_0 t + \varphi(t)]. \quad (4.11)$$

To introduce this expression in (4.10), one needs to calculate the first derivative of η

$$\dot{\eta} = \dot{a} \cos(\omega_0 t + \varphi) - a\omega_0 \sin(\omega_0 t + \varphi) - a\dot{\varphi} \sin(\omega_0 t + \varphi). \quad (4.12)$$

In the method of averaging, it is standard to impose at this stage

$$\dot{a} \cos(\omega_0 t + \varphi) - a\dot{\varphi} \sin(\omega_0 t + \varphi) = 0, \quad (4.13)$$

so that $\dot{\eta} = -a\omega_0 \sin(\omega_0 t + \varphi)$, and one may then proceed to calculate the second derivative of η

$$\ddot{\eta} = -a\omega_0^2 \cos(\omega_0 t + \varphi) - \dot{a}\omega_0 \sin(\omega_0 t + \varphi) - a\omega_0\dot{\varphi} \cos(\omega_0 t + \varphi). \quad (4.14)$$

Inserting the previous expression in (4.10) and noting $\phi = \omega_0 t + \varphi$, one obtains, after some straightforward calculations,

$$\dot{a} \sin \phi + a\dot{\varphi} \cos \phi = -\alpha a \sin \phi + \beta a \sin \phi - 3\kappa_1 a^3 \cos^2 \phi \sin \phi. \quad (4.15)$$

This last equation, together with (4.13), form a linear system. The determinant of this system is $\Delta = 1$, and it is a simple matter to obtain

$$\dot{a} = -\alpha a \sin^2 \phi + \beta a \sin^2 \phi - 3\kappa_1 a^3 \cos^2 \phi \sin^2 \phi, \quad (4.16)$$

$$a\dot{\varphi} = -\alpha a \sin \phi \cos \phi + \beta a \sin \phi \cos \phi - 3\kappa_1 a^3 \cos^3 \phi \sin \phi. \quad (4.17)$$

These equations may then be averaged over a period of oscillation $T = 2\pi/\omega_0$ by taking into account that a and φ on the right-hand side do not vary over that period. The averages on the left-hand side are $[a(t+T) - a(T)]/T$ and $[\varphi(t+T) - \varphi(T)]/T$, which represent the slow variable derivatives with respect to time

$$\frac{da}{dt} = [-\alpha/2 + \beta/2 - 3\kappa_1 a^2/8]a, \quad (4.18)$$

$$a \frac{d\varphi}{dt} = 0. \quad (4.19)$$

According to this model, the phase φ remains constant, while the rate of change of the amplitude a is given by the differential equation (4.18), which may also be written

$$\frac{1}{a} \frac{da}{dt} = \frac{(\beta - \alpha)}{2} - \frac{3}{8} \kappa_1 a^2. \quad (4.20)$$

When $\beta < \alpha$, the right-hand side of this equation is negative and the amplitude decays from its initial value at a rate that is always greater than $(\beta - \alpha)/2$. When $\beta > \alpha$, the previous equation has a stationary solution with a finite amplitude corresponding to a limit cycle

$$a_s = [(4/3)(\beta - \alpha)/(\kappa_1)]^{1/2}. \quad (4.21)$$

This behaviour is typical of a Van der Pol oscillator and one may ask whether the stationary solution is stable. This question can be settled by considering the time evolution of a small perturbation in the amplitude, $a = a_s + \epsilon$. Inserting this expression in the dynamical equation for the amplitude and only retaining first-order terms in ϵ , one obtains, after some straightforward calculations,

$$\frac{d\epsilon}{dt} = -\frac{3}{4} \kappa_1 a_s^2 \epsilon. \quad (4.22)$$

The perturbation in amplitude diminishes exponentially if κ_1 is positive and one concludes that the stationary solution corresponds to a stable limit cycle.

If now the flame response is delayed by a time lag τ_p , such that $\dot{Q}' = \beta^* p(t - \tau_p) - \kappa^* p(t - \tau_p)^3$, one gets the following system for the slow-flow variable equations:

$$\frac{1}{a} \frac{da}{dt} = -\frac{1}{2} [\alpha - (\beta - 3\kappa_1 a^2/4) \cos(\omega_0 \tau_p)], \tag{4.23}$$

$$\frac{d\varphi}{dt} = -\frac{1}{2} (\beta - 3\kappa_1 a^2/4) \sin(\omega_0 \tau_p). \tag{4.24}$$

Compared with (4.18) and (4.19), one can see that the introduction of a time delay in the flame response induces a drift in the slow-flow variable φ and modifies the growth rate and the amplitude of the limit cycle.

However, the problem is that the model used in this section to represent HRR fluctuations as a function of pressure does not allow for an easy and flexible adaptation to experimental flame dynamics data, such as those reported in § 3, figure 4, commonly expressed in terms of FDFs, as a function of slow-flow variables such as the oscillation level. In addition, the amplitude of the stationary solution (4.21) is proportional to the square root of $\beta - \alpha$, and we will see later on (§ 6) that experiments do not comply with this law. For these reason, an alternative HRR model is examined in § 4.2.

4.2. Heat release rate expressed as a function of the oscillation amplitude: $\dot{Q}' = g^*(a)p$

One may now consider a second model that is more flexible and easily adaptable to the experimental data reported in § 3 (figure 4). The choice of this formulation is motivated by the fact that experimental FDF data available in the literature (and used as input in the modelling framework of the kind considered here) are commonly presented as a function of oscillation amplitude level or slow-flow variables (see for instance Ghirardo *et al.* (2016) who use experimental FDF data reported as a function of the level of oscillation or Ghirardo *et al.* (2021) who consider flame response functions expressed in terms of slow-flow variables, like the nature angle, χ). An expression for the HRR as a function of slow-flow variables is better suited for practical applications and corresponds to the natural way of presenting flame dynamics data found in the literature. Investigating this kind of formulation hence enables a simpler comparison between different flame dynamics data.

The central idea is that the ratio between the HRR and pressure fluctuations is a function of the oscillation amplitude level $g^*(a)$, so that $\dot{Q}' = g^*(a)p$. Considering, as in § 4.1, a coupling by a single mode of modal amplitude η ($p = \eta\psi$), the HRR term reads

$$\dot{Q}' = g^*(a)\eta\psi_f. \tag{4.25}$$

To simplify notations, it is convenient to define

$$g(a) = \frac{\gamma - 1}{\Lambda} g^*(a)\psi_f^2, \tag{4.26}$$

and the dynamical equation for η now becomes

$$\ddot{\eta} + \alpha\dot{\eta} + \omega_0^2\eta = g'(a)\dot{a}\eta + g(a)\dot{\eta}. \tag{4.27}$$

Introducing $\phi = \omega_0 t + \varphi$ and noting that $\dot{\eta} = -a\omega_0 \sin(\omega_0 t + \varphi)$, a few calculations yield

$$\dot{a} \left[\sin \phi + \frac{g'(a)a}{\omega_0} \cos \phi \right] + a\dot{\phi} \cos \phi = -\alpha a \sin \phi + g(a)a \sin \phi. \tag{4.28}$$

The system of equations now reads

$$\begin{bmatrix} \cos \phi & -\sin \phi \\ \sin \phi + \frac{g'(a)a}{\omega_0} \cos \phi & \cos \phi \end{bmatrix} \begin{bmatrix} \dot{a} \\ a\dot{\phi} \end{bmatrix} = \begin{bmatrix} 0 \\ -\alpha a \sin \phi + g(a)a \sin \phi \end{bmatrix}, \quad (4.29)$$

and the determinant is

$$\Delta = 1 + \frac{g'(a)a}{\omega_0} \sin \phi \cos \phi. \quad (4.30)$$

System 4.29 may then be solved, yielding

$$\dot{a} = \frac{1}{\Delta} [-\alpha a + g(a)a] \sin^2 \phi, \quad (4.31)$$

$$a\dot{\phi} = \frac{1}{\Delta} [-\alpha a + g(a)a] \sin \phi \cos \phi. \quad (4.32)$$

Averaging over a period is now complicated because the determinant appears in the denominator but it is possible to make an approximation by considering that $g'(a)a/\omega_0 \ll 1$ (see Appendix B, where the order of magnitude of this term is estimated) and write

$$1/\Delta \simeq 1 - \frac{g'(a)a}{\omega_0} \sin \phi \cos \phi. \quad (4.33)$$

Introducing this expression in (4.31) and (4.32) and integrating over a period yields

$$\frac{da}{dt} = \frac{1}{2} [-\alpha + g(a)]a, \quad (4.34)$$

$$\frac{d\phi}{dt} = [-\alpha + g(a)] \frac{[-g'(a)a]}{8\omega_0}. \quad (4.35)$$

These equations indicate that both a and ϕ slowly vary with time. An example of resolution of (4.27) when $g(a) = \beta - \kappa_2 a$ is shown in figure 5(a). The envelope is obtained by integrating (4.34) for the slow variable a . A steady solution exists if $g(a) > \alpha$ in an interval of amplitudes and if $g(a) - \alpha$ vanishes for an amplitude a_s . Here again, one may ask whether the stationary solution corresponds to a stable limit cycle. For this, one can consider a small perturbation in amplitude, such that $a = a_s + \epsilon$ in the vicinity of the stationary solution (or solutions), defined by $g(a_s) - \alpha = 0$. Only retaining first-order terms with respect to ϵ , one obtains

$$\frac{d\epsilon}{dt} = \frac{1}{2} g'(a_s) a_s \epsilon. \quad (4.36)$$

The perturbation vanishes exponentially if $g'(a_s) < 0$ and, in that case, the stationary solution corresponds to a stable limit cycle. However, if $g'(a_s) > 0$, the small perturbation grows exponentially and the stationary solution is unstable.

To fix the ideas, one may consider the case where $g(a)$ is a linearly decreasing function of the amplitude, $f(a) = \beta - \kappa_2 a$. In that case

$$\frac{da}{dt} = \frac{1}{2} (\beta - \alpha - \kappa_2 a)a, \quad (4.37)$$

$$\frac{d\phi}{dt} = (\beta - \alpha - \kappa_2 a) \frac{\kappa_2 a}{8\omega_0}. \quad (4.38)$$

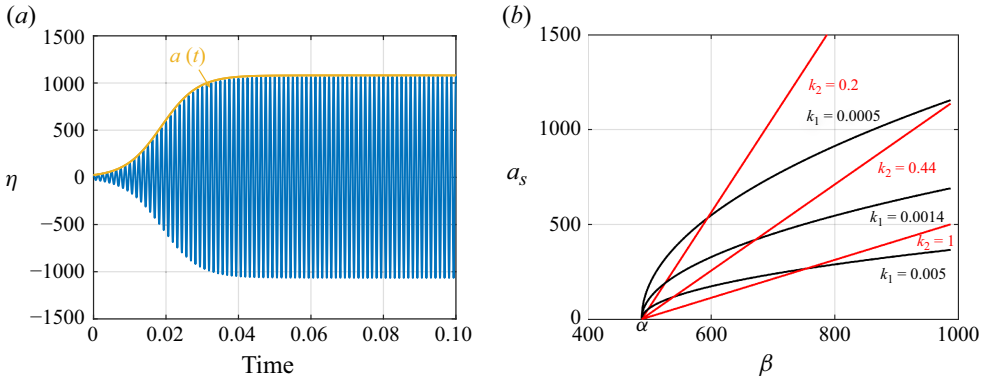


Figure 5. (a) Typical solution of the second-order oscillator (4.27) when $g(a) = \beta - \kappa_2 a$. The envelope is obtained by integrating (4.34) for the slow variable a . (b) Limit-cycle oscillation amplitude a_s as a function of β for the polynomial HRR formulation (black curve) and the new formulation of the form $\dot{Q}' = g^*(a)p$ (red curve) for different values of the saturation coefficients κ_1 and κ_2 . Here, α designates the damping rate of the system.

If $\beta > \alpha$, the stationary solution has an amplitude $a_s = (\beta - \alpha)/\kappa_2$ and the rate of change of φ is positive when the amplitude a is below a_s . This situation corresponds to a positive shift in the frequency of oscillation. We will see later on that the linear relation between $\beta - \alpha$ and the limit-cycle amplitude deduced in this case, is much closer to what is observed experimentally (see the end of § 6 and Appendix E).

It is also instructive to model the situation where the flame response is delayed by a time lag τ_p , and in this case, $\dot{Q}' = g^*(a(t - \tau_p))p(t - \tau_p)$. Since the order of magnitude of the delay is well below that of a period of oscillation, one may assume that $a(t - \tau_p) \approx a(t)$ (a is a slow-flow variable assumed constant over a period of oscillation) and write $\dot{Q}' = g^*(a)p(t - \tau_p)$. For the pressure field of (4.7), one has

$$\dot{Q}' = g^*(a)\eta(t - \tau_p)\psi_f. \tag{4.39}$$

Introducing $g(a) = [(\gamma - 1)/\Lambda]g^*(a)\psi_f^2$ and applying the method of averaging, one obtains the following slow-flow variable equations:

$$\frac{1}{a}\dot{a} = -\frac{1}{2}[\alpha - g(a) \cos \omega_0 \tau_p] + \frac{g'(a)a}{\omega_0} \left[\frac{3}{8}\alpha \sin \omega_0 \tau_p - \frac{1}{8}g(a) \sin 2\omega_0 \tau_p \right], \tag{4.40}$$

$$\dot{\varphi} = -\frac{1}{2}g(a) \sin \omega_0 \tau_p + \frac{1}{8} \frac{g'(a)a}{\omega_0} [\alpha \cos \omega_0 \tau_p - g(a) \cos 2\omega_0 \tau_p]. \tag{4.41}$$

One checks that (4.34) and (4.35) are retrieved when $\tau_p = 0$. Noting, in addition, that $g'(a)a/\omega_0 \ll 1$, one finds that a non-zero delay induces a change in the gain of the form $+(1/2)g(a) \cos \omega_0 \tau_p$ and a shift in frequency $\Delta\omega$ with respect to ω_0 such that $\Delta\omega \simeq -(1/2)g(a) \sin \omega_0 \tau_p$. Using these two expressions, one retrieves the result, verified experimentally, and quoted in § 2, that the relative shift in frequency is generally quite small.

At this stage, it is also worth plotting the limit-cycle amplitudes a_s as a function of β for the two HRR formulations ($\dot{Q}' = \beta p - \kappa_1 p^3$ and $\dot{Q}' = (\beta - \kappa_2 a)p$) and for different values of the saturation constants κ_1 and κ_2 , as shown in figure 5(b). One may note that, in both cases, the effective growth rate is such that $\omega'_i(0) = 1/2(\beta - \alpha)$. The diagram shown in figure 5 is also reminiscent of the one plotted in Latour *et al.* (2024a), (figure 16 of that reference), where the limit-cycle amplitudes obtained were found to be in a quasi-linear

relation with the effective linear growth rate. We will see later on that this behaviour can be theoretically explained with the model derived in what follows.

Finally, it is interesting to note that, by injecting a quadratic expression of the form $g(a) = \beta - \kappa a^2$ in (4.40) and (4.41) and remembering that the term associated with $g'(a)a/\omega_0$ is negligible, one retrieves (4.23) and (4.24), obtained for the HRR model discussed in §4.1. However, the HRR formulation of the form $\dot{Q}' = g^*(a)p$ has the advantage of being flexible and easily adaptable to pressure-based FDF data reported in terms of slow-flow variables (or velocity based FDFs if an impedance is used).

5. Theoretical framework for investigating injectors' staging effects

A representation of the HRR as a function of pressure fluctuations is identified in §4.2 and suitably accounts for the experimentally measured pressure-based FDFs. To use this description in the analysis of a set of staging patterns obtained by mixing different injectors in MICCA, it is natural to consider the dynamics of oscillations through a set of slow-flow variable equations (SFVE). The objective is to see if the new FDF representation, when inserted in the SFVE, can be used to retrieve the experimental data gathered in MICCA for the large number of staging patterns reported by Latour *et al.* (2024a). We specifically wish to see if it is possible to obtain limit-cycle amplitudes and modal characteristics (like the spin ratio and the nodal line location) corresponding to the staging configurations shown in figure 6.

The starting point is the model proposed by Ghirardo *et al.* (2016), where an annular combustor with N acoustically compact flames, each modelled with a FDF through an operator \mathcal{Q} , is considered. The main steps leading to the derivation of the equations for slow-flow variables are recalled. The obtained analytical expressions are then used in a second step to predict the limit-cycle oscillation amplitude, modal nature and nodal line location, and these predictions are finally compared with the experimental observations.

5.1. Governing equations

The starting point is the non-homogeneous wave equation derived in §4.1

$$\frac{\partial^2 p}{\partial t^2} - \nabla \cdot c^2 \nabla p = S - \alpha \frac{\partial p}{\partial t}. \quad (5.1)$$

The source term S is now expressed as the sum of the contributions of N acoustically compact flames behaving like point sources

$$S = \sum_{j=1}^N (\gamma - 1) \frac{\partial \dot{q}'_j}{\partial t}, \quad (5.2)$$

with \dot{q}'_j the HRR fluctuations at flame j , expressed as

$$\dot{q}'_j = \dot{Q}'_j \delta(\mathbf{x} - \mathbf{x}_j), \quad (5.3)$$

where δ is the Dirac function centred at the position \mathbf{x}_j of the j th flame and \dot{Q}'_j the HRR fluctuation integrated over the volume of that flame.

The modal eigenfunctions pertaining to the MICCA annular combustor are discussed in Appendix C. In what follows, only two eigenmodes will be retained in the expression of the pressure field of (4.4), both corresponding to the same eigenfrequency

$$p = \eta_1(t)\psi_1(\mathbf{x}) + \eta_2(t)\psi_2(\mathbf{x}), \quad (5.4)$$

● Injector U ● Injector S

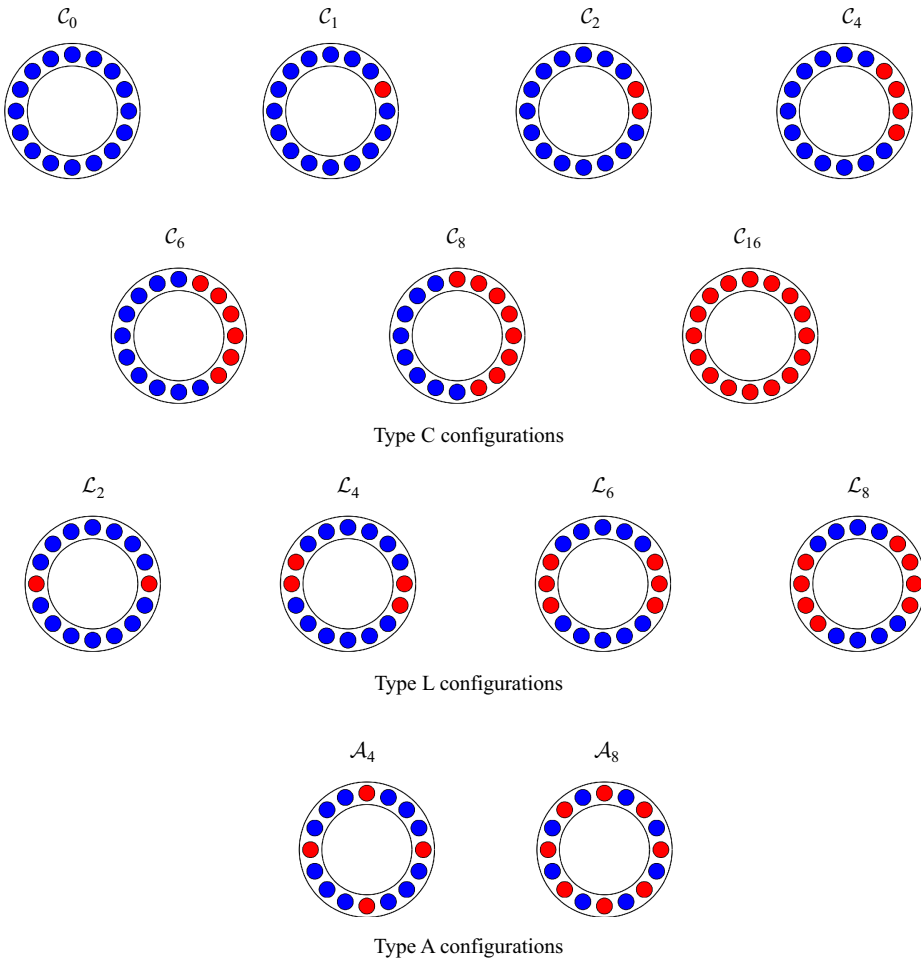


Figure 6. Injector configurations investigated.

with ψ_1 and ψ_2 , two orthogonal 1A1L modes, expressed as $\psi_1(x) = \cos(\theta)\psi_f$ and $\psi_2(x) = \sin(\theta)\psi_f$, ψ_f representing the 1L axial wave function evaluated at the flame barycentre position, x_f ($\psi_{1L}(x_f) = \cos[\pi x_f/(2l')]$), presented in § 2), and η_1 and η_2 corresponding to the associated modal amplitudes.

As in § 4 and discussed in the supplementary material, the coupling with the injector ports is not taken into account: the changes in section induced by the injection units decouple the chamber and the plenum cavity and there is no plenum mode matching the eigenfrequency of the 1A1L chamber mode, eliminating the possibility of veering.

Using the orthogonality of the eigenmodes basis and integrating over the volume of the combustor, one gets the following equation for the amplitude η_n of the n th mode:

$$\ddot{\eta}_n + \alpha \dot{\eta}_n + \omega_n^2 \eta_n = \frac{1}{\Lambda_n} \int_V S \psi_n dV, \quad (5.5)$$

where $n = 1, 2$ and $\Lambda_n = \int_V \psi_n \psi_n^* dV$ is the normalization factor. It is shown in Appendix C that, for azimuthal modes having a non-zero azimuthal number n , $\Lambda_n = V/4$,

where V is the combustor volume. Injecting (5.2) and (5.3) in the right-hand side of (5.5), one finally obtains

$$\frac{1}{\Lambda_n} \int_V S \psi_n dV = \frac{(\gamma - 1)}{\Lambda_n} \sum_{j=1}^N \frac{\partial \dot{Q}'_j}{\partial t} \psi_n(x_j). \quad (5.6)$$

5.2. Heat release rate model

One now needs an analytical expression for the HRR response of the flame to acoustic disturbances. As discussed in § 4.2, the HRR \dot{Q}'_j at the j th flame is now expressed as a function \mathcal{G} of the local amplitude, at the angular frequency of interest ω_0 and local pressure with a time delay

$$\dot{Q}'_j = \mathcal{G}(\Pi_j, \omega_0) p_j(t - \tau_p), \quad (5.7)$$

where the local amplitude at flame j is the slow-flow variable, $\Pi_j = (p_{rms})_j / (\rho U_b^2)$, which will be expressed later in terms of the variables of interest. It is also shown in § 5.3 how \mathcal{G} is linked to the pressure based FDF at the frequency ω_0 of interest.

The local amplitude Π_j being a slow-flow variable assumed constant over a period of oscillation and, in addition, as the terms associated with the $\dot{\mathcal{G}}$ term were shown to be negligible in the SFVE in § 4, one may write

$$\frac{\partial \dot{Q}'_j}{\partial t} = \mathcal{G}(\Pi_j, \omega_0) \dot{p}_j(t - \tau_p), \quad (5.8)$$

and the governing equations projected on the modes ψ_1 and ψ_2 read

$$\begin{aligned} \ddot{\eta}_1 + \alpha \dot{\eta}_1 + \omega_0^2 \eta_1 &= \frac{\gamma - 1}{\Lambda} \sum_{j=1}^N \mathcal{G}(\Pi_j, \omega_0) [\dot{\eta}_1(t - \tau_p) \psi_1(x_j) + \dot{\eta}_2(t - \tau_p) \psi_2(x_j)] \psi_1(x_j) \\ \ddot{\eta}_2 + \alpha \dot{\eta}_2 + \omega_0^2 \eta_2 &= \frac{\gamma - 1}{\Lambda} \sum_{j=1}^N \mathcal{G}(\Pi_j, \omega_0) [\dot{\eta}_1(t - \tau_p) \psi_1(x_j) + \dot{\eta}_2(t - \tau_p) \psi_2(x_j)] \psi_2(x_j). \end{aligned} \quad (5.9)$$

5.3. Expression of the HRR using the pressure-based FDF

One now seeks to link the time domain expression involving the function \mathcal{G} to the pressure-based FDF, $\mathcal{F}_p = G_{p_j}(\Pi_j, \omega) e^{i\varphi_{p_j}}$, as defined in (3.1), where Π_j is the reduced pressure oscillation root-mean-square (r.m.s.) value and G_{p_j} and φ_{p_j} are the FDF gain and phase of the j th flame. It is important to remember at this point that the dynamics of the system only takes place around the eigenfrequency of the 1A1L mode, identified to be involved in the combustion/acoustics coupling in MICCA. One hence looks for a solution of the pressure field in the form

$$p_j = A_1 \cos(\omega_0 t + \varphi_1) \psi_1(x_j) + A_2 \cos(\omega_0 t + \varphi_2) \psi_2(x_j), \quad (5.10)$$

where A_1, A_2, φ_1 and φ_2 are slowly varying compared with the oscillation period $T = 2\pi/\omega_0$. One can also identify from (5.4), $\eta_1(t) = A_1 \cos(\omega_0 t + \varphi_1)$ and $\eta_2 = A_2 \cos(\omega_0 t + \varphi_2)$.

It is convenient to introduce at this stage the analytic signals \hat{p}_j and \hat{Q}'_j , such that the pressure and HRR signals are the real parts of these complex quantities: $p_j = \text{Re}(\hat{p}_j)$

and $\dot{Q}'_j = \text{Re}(\hat{Q}_j)$. Now, the complex pressure signal may be written in terms of the eigenmodes ψ_1 and ψ_2 as

$$\hat{p}_j = \hat{\eta}_1 \psi_1(x_j) + \hat{\eta}_2 \psi_2(x_j), \quad (5.11)$$

where the complex amplitudes $\hat{\eta}_1$ and $\hat{\eta}_2$ are expressed as $\hat{\eta}_1 = A_1 \exp(-i\omega_0 t - i\varphi_1)$ and $\hat{\eta}_2 = A_2 \exp(-i\omega_0 t - i\varphi_2)$.

The complex HRR signal \hat{Q}_j at flame j may now be linked to the complex pressure signal by the describing function \mathcal{F}_p , expressed in terms of a gain and a phase and considered at the angular frequency ω_0 :

$$\hat{Q}_j = G_{p_j}(\Pi_j, \omega_0) e^{i\varphi_{p_j}} \frac{\dot{Q}_0}{\rho U_b^2} \hat{p}_j. \quad (5.12)$$

This is just the describing function extension of a standard result of linear system theory which indicates that, when the input to the system is a complex sinusoidal signal at the frequency ω_0 , its complex signal output features the same frequency and is equal to the product of the transfer function at that frequency by the complex signal input. Injecting (5.11) in (5.12), one obtains

$$\hat{Q}_j = G_{p_j}(\Pi_j, \omega_0) \frac{\dot{Q}_0}{\rho U_b^2} [\hat{\eta}_1 e^{i\varphi_{p_j}} \psi_1(x_j) + \hat{\eta}_2 e^{i\varphi_{p_j}} \psi_2(x_j)]. \quad (5.13)$$

One may now deduce the HRR signal by taking the real part of the complex HRR signal in (5.13)

$$\begin{aligned} \dot{Q}'_j &= G_{p_j}(\Pi_j, \omega_0) \frac{\dot{Q}_0}{\rho U_b^2} [A_1 \cos(\omega_0 t + \varphi_1 - \varphi_{p_j}) \psi_1(x_j) \\ &\quad + A_2 \cos(\omega_0 t + \varphi_2 - \varphi_{p_j}) \psi_2(x_j)]. \end{aligned} \quad (5.14)$$

It is here convenient to define $\tau_{p_j} = \varphi_{p_j} / \omega_0$ and write the previous expression as

$$\begin{aligned} \dot{Q}'_j &= G_{p_j}(\Pi_j, \omega_0) \frac{\dot{Q}_0}{\rho U_b^2} [A_1 \cos(\omega_0(t - \tau_{p_j}) + \varphi_1) \psi_1(x_j) \\ &\quad + A_2 \cos(\omega_0(t - \tau_{p_j}) + \varphi_2) \psi_2(x_j)]. \end{aligned} \quad (5.15)$$

One identifies in this expression the delayed pressure signal $p_j(t - \tau_{p_j})$ so that one may write

$$\dot{Q}'_j = G_{p_j}(\Pi_j, \omega_0) \frac{\dot{Q}_0}{\rho U_b^2} p_j(t - \tau_{p_j}). \quad (5.16)$$

Slow-flow variables $A_1, A_2, \varphi_1, \varphi_2$ and Π_j being assumed constant over a period of oscillation, the time derivative of the HRR simply involves the rate of change of the pressure delayed by τ_{p_j}

$$\frac{\partial \dot{Q}'_j}{\partial t} = G_{p_j}(\Pi_j, \omega_0) \frac{\dot{Q}_0}{\rho U_b^2} \dot{p}_j(t - \tau_{p_j}). \quad (5.17)$$

Comparing (5.8) and (5.17), one finds that

$$\mathcal{G}(\Pi_j, \omega_0) = G_{p_j}(\Pi_j, \omega_0) \frac{\dot{Q}_0}{\rho U_b^2} \quad (5.18)$$

and the dynamical system of (5.5) finally becomes

$$\begin{aligned} \ddot{\eta}_1 + \alpha \dot{\eta}_1 + \omega_0^2 \eta_1 &= \frac{\gamma - 1}{\Lambda} \sum_{j=1}^N G_{p_j} \frac{\dot{Q}_0}{\rho U_b^2} [\dot{\eta}_1(t - \tau_{p_j}) \psi_1(x_j) + \dot{\eta}_2(t - \tau_{p_j}) \psi_2(x_j)] \psi_1(x_j) \\ \ddot{\eta}_2 + \alpha \dot{\eta}_2 + \omega_0^2 \eta_2 &= \frac{\gamma - 1}{\Lambda} \sum_{j=1}^N G_{p_j} \frac{\dot{Q}_0}{\rho U_b^2} [\dot{\eta}_1(t - \tau_{p_j}) \psi_1(x_j) + \dot{\eta}_2(t - \tau_{p_j}) \psi_2(x_j)] \psi_2(x_j), \end{aligned} \quad (5.19)$$

where $G_{p_j} = G_{p_j}(\Pi_j, \omega_0)$ and the local oscillation amplitude Π_j , expressed in terms of the slow-flow variables, reads

$$\Pi_j = \frac{1}{\rho U_b^2 \sqrt{2}} [A_1^2 \psi_1^2 + A_2^2 \psi_2^2 + 2A_1 A_2 \psi_1 \psi_2 \cos(\varphi_2 - \varphi_1)]^{1/2}. \quad (5.20)$$

Using, in addition, the standard hypothesis of the method of averaging, the time derivative of the amplitude η is

$$\dot{\eta}_k = -A_k(t) \omega_0 \sin(\omega_0 t + \varphi_k) \text{ for } k = 1, 2, \quad (5.21)$$

and one can express the slow-flow variables as a function of η_k and $\dot{\eta}_k$

$$A_k = \left[\eta_k^2 + \left(\frac{\dot{\eta}_k}{\omega_0} \right)^2 \right]^{1/2}, \text{ and } A_j A_k \cos(\varphi_j - \varphi_k) = \eta_j \eta_k + \frac{1}{\omega_0^2} \dot{\eta}_j \dot{\eta}_k. \quad (5.22)$$

The dynamics can hence be described by two coupled second-order oscillators. The coupling between the two eigenmodes appears on the right-hand side of these two equations, corresponding to the projection of the source term S on each eigenmode. Equations (5.19) can be solved directly, as done, for instance, in Noiray *et al.* (2011). The integration is here carried out by making use of the FDF representation obtained in § 3. Typical examples of the direct integration of 5.19 are provided for staging patterns \mathcal{C}_0 , \mathcal{C}_4 , \mathcal{L}_4 and \mathcal{A}_4 and shown in figure 7 in the form of plots in the (η_1, η_2) plane. Circular trajectories in this plane found for \mathcal{C}_0 or for \mathcal{A}_4 indicate that the oscillation at the limit cycle takes the form of a spinning mode. The elongated trajectories characterizing \mathcal{C}_4 or \mathcal{L}_4 are typical of standing mode oscillations reflecting the symmetry breaking induced by the placement of four S injectors.

5.4. Slow-flow equations

A further understanding of the system's dynamics may be gained by deriving a set of equations for the slow-flow variables A_1 , A_2 , φ_1 and φ_2 using the method of averaging. Solutions of (5.19) are now sought in the standard form

$$\begin{aligned} \eta_k &= A_k(t) \cos(\omega_0 t + \varphi_k) \\ \dot{\eta}_k &= -A_k(t) \omega_0 \sin(\omega t + \varphi_k) \text{ for } k = 1, 2. \end{aligned} \quad (5.23)$$

Using the same procedure as that described in § 4 and integrating over a period of oscillation $T = 2\pi/\omega_0$, this system yields the following equations for the slow-flow variables A_1 , A_2 , φ_1 and φ_2 :

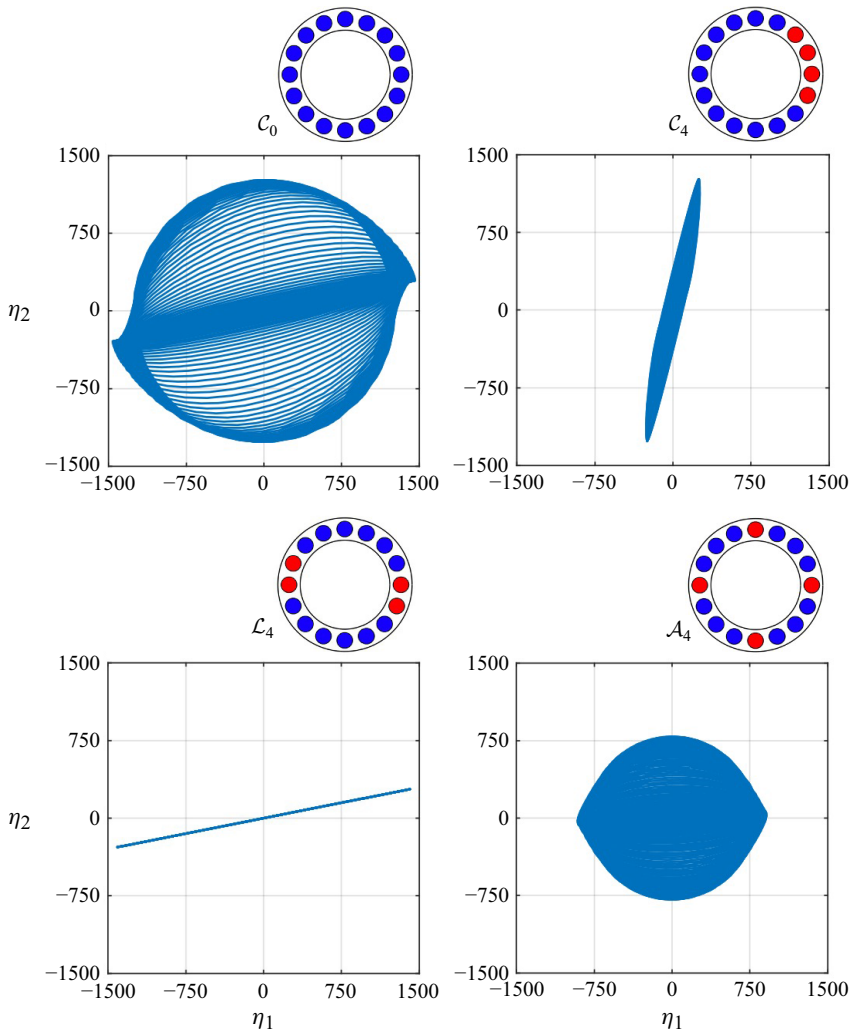


Figure 7. Direct integration of the ordinary differential system with delay (5.19), for an initial condition $[\eta_1 = 75, \dot{\eta}_1 = 50, \eta_2 = 15, \dot{\eta}_2 = 10]$, for configurations C_0, C_4, L_4 and A_4 .

$$\begin{aligned} \dot{A}_1 &= -\frac{\alpha}{2}A_1 + \frac{\gamma - 1}{2\Lambda} \frac{\dot{Q}_0}{\rho U_b^2} \sum_{j=1}^N G_{p_j} [A_1 \cos(\varphi_{p_j})\psi_1(x_j) + A_2 \cos(\varphi_{p_j} \\ &\quad + \varphi_{12})\psi_2(x_j)]\psi_1(x_j) \\ \dot{A}_2 &= -\frac{\alpha}{2}A_2 + \frac{\gamma - 1}{2\Lambda} \frac{\dot{Q}_0}{\rho U_b^2} \sum_{j=1}^N G_{p_j} [A_2 \cos(\varphi_{p_j})\psi_2(x_j) + A_1 \cos(\varphi_{p_j} \\ &\quad + \varphi_{21})\psi_1(x_j)]\psi_2(x_j) \\ A_1\dot{\varphi}_1 &= \frac{\gamma - 1}{\Lambda} \frac{\dot{Q}_0}{\rho U_b^2} \sum_{j=1}^N G_{p_j} [-A_1 \sin(\varphi_{p_j})\psi_1^2(x_j) + A_2 \sin(\varphi_{21} - \varphi_{p_j})\psi_1(x_j)\psi_2(x_j)] \end{aligned}$$

$$A_2 \dot{\varphi}_2 = \frac{\gamma - 1}{\Lambda} \frac{\dot{Q}_0}{\rho U_b^2} \sum_{j=1}^N G_{p_j} [-A_2 \sin(\varphi_{p_j}) \psi_2^2(x_j) + A_1 \sin(\varphi_{12} - \varphi_{p_j}) \psi_1(x_j) \psi_2(x_j)]. \quad (5.24)$$

In these equations $\varphi_{12} = \varphi_1 - \varphi_2$, $\varphi_{21} = \varphi_2 - \varphi_1$ and the gains and phases, $G_{p_j} = G_j(\Pi_j, \omega_0)$ and $\varphi_{p_j} = \varphi_{p_j}(\Pi_j, \omega_0)$, correspond to the flames established by the different injectors, with $\Pi_j = (p_{rms})_j / (\rho U_b^2)$, the dimensionless pressure amplitude at flame j , which is expressed in terms of the slow-flow variables in (5.20).

It is also interesting to deduce an evolution equation for the difference $\varphi_1 - \varphi_2$. This can be done by multiplying the third equation in the set (5.24) by A_2 and subtracting the fourth equation in this set after multiplication by A_1 . This yields

$$\begin{aligned} A_1 A_2 (\dot{\varphi}_1 - \dot{\varphi}_2) &= \frac{(\gamma - 1)}{\Lambda} \frac{\dot{Q}_0}{\rho U_b^2} \sum_{j=1}^N G_{p_j} \left\{ A_1 A_2 \sin(\varphi_{p_j}) [\psi_2^2(x_j) - \psi_1^2(x_j)] \right. \\ &\quad - A_1^2 \sin(\varphi_1 - \varphi_2 - \varphi_{p_j}) \psi_1(x_j) \psi_2(x_j) \\ &\quad \left. + A_2^2 \sin(\varphi_2 - \varphi_1 - \varphi_{p_j}) \psi_1(x_j) \psi_2(x_j) \right\}. \quad (5.25) \end{aligned}$$

A comprehensive discussion on the theoretical conditions for the stability of fixed standing and spinning solutions of the system formed by (5.24) can be found in Ghirardo *et al.* (2016). Additional terms due to turbulence-induced acoustic forcing were not considered in the present work, because, as will be seen in § 5.5, the dynamical equations, in the form proposed in (5.24), enable us to reasonably retrieve the features observed experimentally, which are mainly dominated by symmetry-breaking effects induced by injectors' staging. There is, however, one exception, in the special case where all injectors are of the same kind: we will see that the dynamical equations predict a limit cycle in the form of a purely spinning wave, while experiments indicate that the system continuously switches between spinning modes and mixed modes of various types. In that case, the stochastic term representing turbulent disturbances might probably be necessary to obtain a suitable match with observations (on that point see Ghirardo *et al.* 2018).

5.5. Application to staging patterns in MICCA-spray

The system of ordinary differential equations (ODEs) obtained in § 5.4 is now solved for different configurations mixing U- and S-injectors in MICCA, shown in figure 6. For all the staging patterns tested, the instability frequencies lie between 775 and 820 Hz and the oscillation amplitudes between 100 and 1400 Pa. Further details on the experimental results may be found in Latour *et al.* (2024a).

Expressions for $G_{p_j}(\Pi_j, \omega_0)$ and $\varphi_{p_j}(\Pi_j, \omega_0)$ are those deduced from experimental data for the two injection units U and S, collected for a range of frequencies close to the eigenfrequency of the 1AIL mode of the MICCA combustor and reported in § 3. One can reasonably model the gain of the pressure-based FDF as $G_{p_j} = \beta - \kappa \Pi_j$, as discussed in § 3. The coefficients β and κ for injectors U and S are deduced from a linear regression of the $G_p = G_p(\Pi)$ data points. The phases, φ_S and φ_U , are assumed to be constant and equal to the mean value, as shown by the experimental results reported in figure 4, where the phases for the two injectors take nearly constant values throughout the range of pressure amplitudes tested. Noting that the damping rate α describes the rate of change in acoustic energy (i.e. of pressure squared), the damping rate used for the numerical integration is assigned a value that is twice that obtained by Latour *et al.* (2024b), where the damping rate for the pressure is extracted from direct measurements of the Rayleigh source term

Pressure-based FDF for injector U	$G_p^U = 0.92 - 0.95\Pi_j$	$\varphi_p^U = 0.30 \text{ rad}$
Pressure-based FDF for injector S	$G_p^S = 0.28 - 0.19\Pi_j$	$\varphi_p^S = 0.28 \text{ rad}$
Damping rate	$\alpha = 950 \text{ s}^{-1}$	

Table 2. Pressure-based FDFs and damping rate used in the numerical simulations.

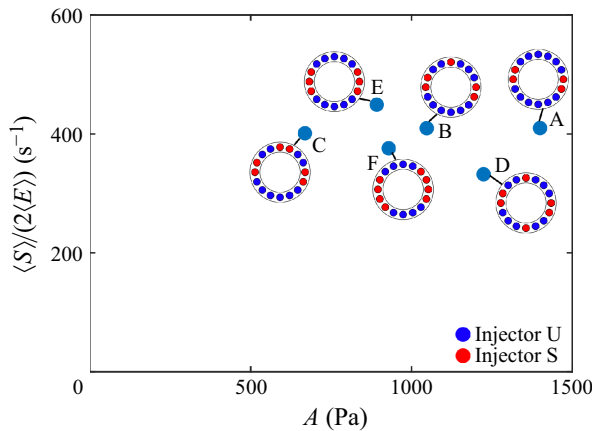


Figure 8. Damping rate values as a function of the oscillation level A obtained from source term and acoustic energy estimates in MICCA during self-sustained limit-cycle oscillations for different staging configurations Latour *et al.* (2024b). The annular combustor is operated at a thermal power $\mathcal{P} = 118 \text{ kW}$ and an equivalence ratio $\phi = 0.9$.

while operating the MICCA combustor at limit cycle. It is also assumed that the damping rate value does not change with the staging pattern and may be represented by a constant value.

As pointed out by a reviewer, there are cases where the damping depends nonlinearly on the level of oscillation. For example, damping by Helmholtz resonators is a function of the level of oscillation, as shown by Zinn & Lores (1972) or Čosić, Reichel & Paschereit (2012). The nonlinearity is, in this case, linked to the vortex shedding from the resonator outlet. The use of perforated liners or quarter wave cavities also introduces nonlinearities as indicated for example by Schuller *et al.* (2009). However, MICCA is not equipped with such devices and the damping nonlinearity is less probable. In addition, the damping rates of acoustic energy estimated in MICCA from energy balance considerations at various limit-cycle amplitudes for a range of limit-cycle oscillation levels (670–1400 Pa) by Latour *et al.* (2024b) show no amplitude dependence, as can be seen in figure 8. There are only minor variations in the damping rate for the different oscillation levels and one may safely conclude that nonlinearities need not be taken into consideration.

Using the parameters gathered in table 2, the differential equations are integrated with the MATLAB ode45 solver. Typical results shown in figure 9 pertain to the four staging patterns C_0 , C_4 , \mathcal{L}_4 and A_4 .

In the C_0 case, the amplitudes A_1 and A_2 grow to the limit cycle in approximately 25 ms and take the same value, while the phase difference $\varphi_1 - \varphi_2$ tends to $\pi/2$, indicating that the mode is a spinning wave. For configurations C_4 and \mathcal{L}_4 , the amplitudes reach constant levels while the phase difference $\varphi_1 - \varphi_2$ tends to zero. The oscillation now corresponds to a standing mode. The anti-nodal line angle θ_0 may be deduced from the values of

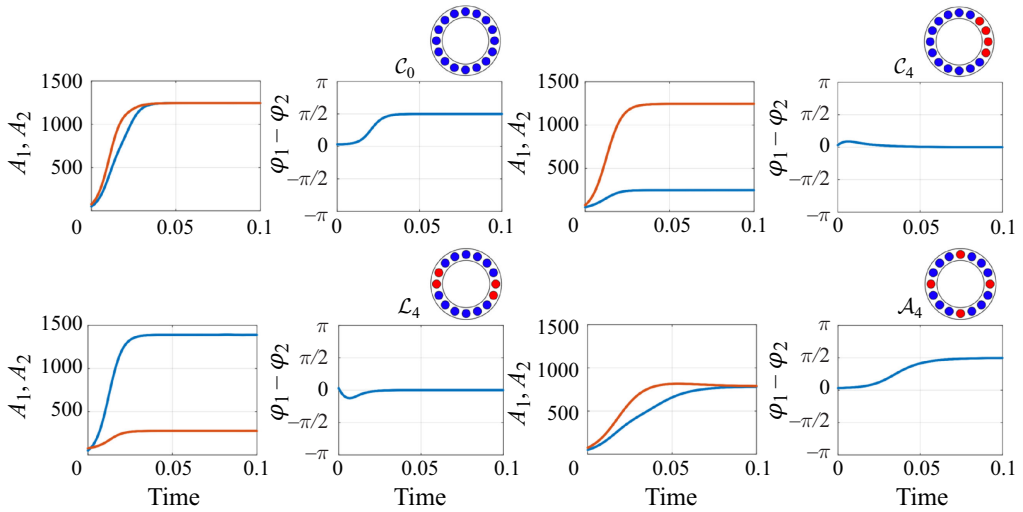


Figure 9. Slow-flow variables A_1 , A_2 and $\varphi_1 - \varphi_2$ time evolutions for configurations C_0 , C_4 , L_4 and A_4 , obtained from the resolution of the ordinary differential equations for the initial conditions $A_1 = 50$ Pa, $A_2 = 75$ Pa, $\varphi_1 - \varphi_2 = 0.1$ rad.

A_1 and A_2 at limit cycle, using the expression $\theta_0 = \arccos[A_1/(A_1^2 + A_2^2)^{1/2}]$. The nodal line found analytically is aligned with the diameter joining the two groups of S-injectors in diametrically opposed locations for L_4 and passes at equal distance of the four S injectors in configuration C_4 . These analytical results correspond to those found experimentally (Latour *et al.* 2024a). Finally, in case A_4 , the growth in amplitude is less rapid than in the C_0 case and the levels at limit cycle are also lower. Similarly to configuration C_0 , A_1 is equal to A_2 while $\varphi_1 - \varphi_2$ tends to $\pi/2$, which correspond to a spinning wave.

It is next interesting to examine the predicted limit-cycle amplitudes and compare them with the values measured experimentally. This comparison may be carried out by making use of the link between the amplitude $A = (A_+^2 + A_-^2)^{1/2}$ that is used in the experimental determination of the limit-cycle amplitudes (see § 2, (2.3) and Latour *et al.* 2024a) and the amplitudes A_1 and A_2 of the eigenmodes ψ_1 and ψ_2 , intervening in (5.24). It is shown in Appendix D that

$$A = (A_+^2 + A_-^2)^{1/2} = \frac{1}{2^{1/2}}(A_1^2 + A_2^2)^{1/2}. \quad (5.26)$$

The predicted limit-cycle oscillation amplitudes A , deduced by solving the slow-flow equations for A_1 and A_2 and making use of 5.26, are displayed in figure 10. The amplitude A decreases when the number of S-injectors is increased and the trends corresponding to type C arrangements clearly differ from those pertaining to L configurations. A comparison with the experimental data from Latour *et al.* (2024a) is carried out in figure 10(b,c,d) where the C , L and A configurations appear in three separate graphs. The match obtained between experimental data and model prediction is, despite some differences, quite satisfactory. The limit-cycle amplitudes cover the same range with a maximum value of slightly less than 1500 Pa. Configurations C_8 and A_8 , which are experimentally stable, are suitably predicted by the model as having a low level of oscillation. The decrease in amplitude observed when the staging patterns is evolving from C_0 to C_8 is well retrieved but the calculated amplitudes are slightly higher than those measured experimentally.

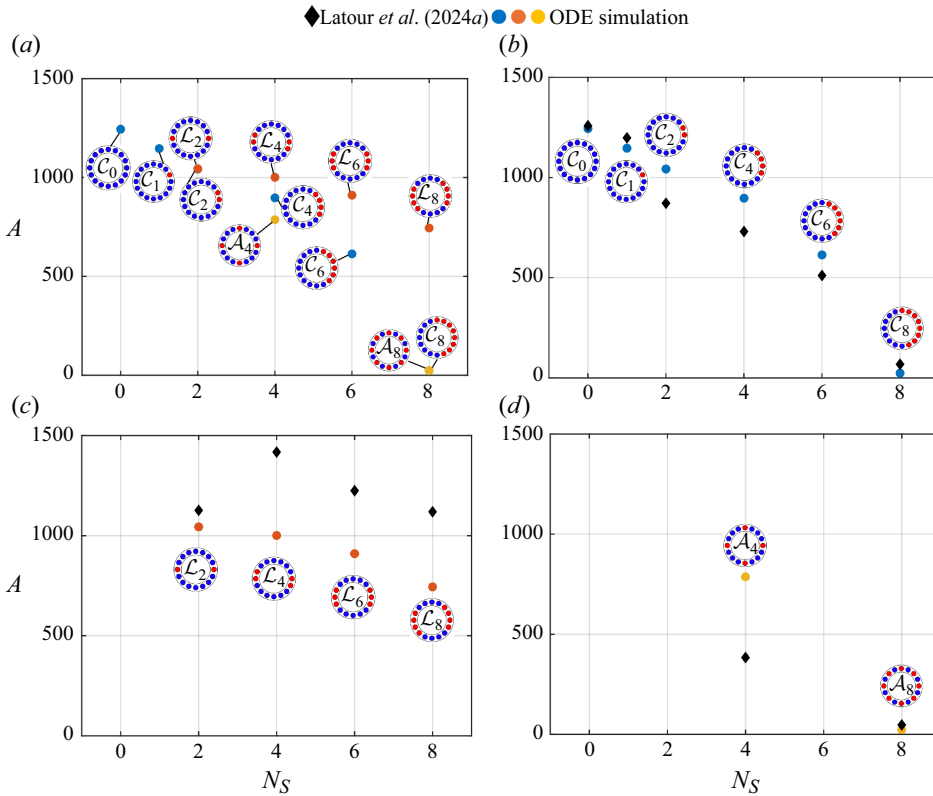


Figure 10. (a) Limit-cycle oscillation amplitudes obtained by integrating the system of ODEs for the slow-flow variables for the three types of staging configurations investigated (type C, L and A). (b,c,d) Comparison of the limit-cycle oscillation amplitudes measured experimentally (Latour *et al.* 2024a) and obtained by solving the system of ODEs for the slow-flow variables for type C (b), L (c) and A (d) configurations. Here N_S corresponds to the number of S-injectors.

The trends observed experimentally for the L-type staging patterns, where the limit-cycle amplitude levels decrease more slowly than for type C configurations as the number of S-injectors is augmented, are also found with the model, although larger discrepancies are observed between experimental data and simulation for these configurations. The greatest differences in limit-cycle amplitudes are found for C₄, L₄ and A₄. This may be due to a different damping rate value for these staging arrangements (Latour *et al.* 2024b) that is not accounted for in the modelling. It is also possible that some adjustment of the gain G_p^S corresponding to the S-injectors might have improved the prediction, but no attempt was made to go in that direction. As indicated in § 3, the gain and phase values for S-injectors are less well determined because these units are located in regions where the oscillation level is low and this influences the measurement precision. Another possibility could be that the gain G_p is influenced to some extent by the nature of the mode as inferred by Nygård, Ghirardo & Worth (2021) and Ghirardo *et al.* (2021), and that this might have to be accounted for in the pressure-based FDF formulation. However, although some discrepancies exist between experimental data and model predictions, this is perhaps the first time where calculations are shown to be capable of predicting limit-cycle levels of oscillation for a large set of experiments.

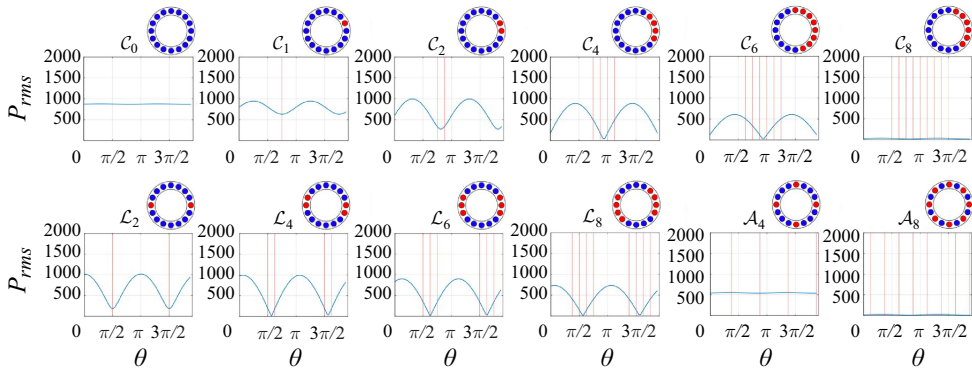


Figure 11. Root mean square of the pressure distribution as a function of the azimuthal position θ obtained from the numerical integration of the ODEs for the slow-flow variables. The red vertical lines correspond to S-injectors positions.

It is next interesting to examine the distribution of the r.m.s. of the pressure field as a function of the azimuthal position deduced from the numerical integration of the slow-flow equations. This distribution is shown in figure 11 for all the staging configurations. The first row in this figure corresponds to \mathcal{C} configurations. For \mathcal{C}_0 , where all injectors are of the U-type, the r.m.s. pressure distribution is uniform, as expected for a spinning mode. As S-injectors are being added to replace U-injectors, the r.m.s. pressure distribution features two maximum and two minimum values. The minimum is reached at the location of the S-injector (case \mathcal{C}_1) or on the diameter passing through the centre of the \mathcal{C} configuration as exemplified by \mathcal{C}_2 , \mathcal{C}_4 and \mathcal{C}_6 . In the last two cases, the minimum r.m.s. pressure is close to zero, corresponding to a standing mode. In case \mathcal{C}_8 , the calculated level of oscillation is very low, indicating that the system is stable. The second row shows the r.m.s. pressure distributions for \mathcal{L} and \mathcal{A} cases. The minimum values are observed on the diameter that passes through the S-injectors (case \mathcal{L}_2) or on the median diameter of the S-injector configurations (\mathcal{L}_4 , \mathcal{L}_6 , \mathcal{L}_8). In the last three cases, the minimum value is close to zero, a clear signature of a standing mode. The cases \mathcal{A}_4 and \mathcal{A}_8 feature a uniform distribution of r.m.s. pressure as the symmetry is not broken by the presence of the 4 or 8 S-injectors. In case \mathcal{A}_4 , the amplitude is reduced but not to the point observed experimentally (this configuration is marginally unstable). In \mathcal{A}_8 , the level is quite low and the system is stable.

The previous calculations already show typical consequences of the breaking of symmetry in various configurations. These features generally retrieve those found in experiments. For example, it is known that the presence of a single S-injector in \mathcal{C}_1 is insufficient to break the symmetry and the pressure distribution only shows weak undulations. In cases \mathcal{C}_4 and \mathcal{C}_6 and in arrangements \mathcal{L}_4 , \mathcal{L}_6 and \mathcal{L}_8 , symmetry is broken, giving rise to a standing mode and this agrees well with what is found experimentally (see Latour *et al.* 2024b). It is, however, interesting to pursue the examination of the nature of the unstable mode by computing the spin ratio, initially defined by Bourgouin *et al.* (2013) in terms of azimuthal wave amplitudes A_+ , A_- as

$$s_r = \frac{A_+ - A_-}{A_+ + A_-}. \quad (5.27)$$

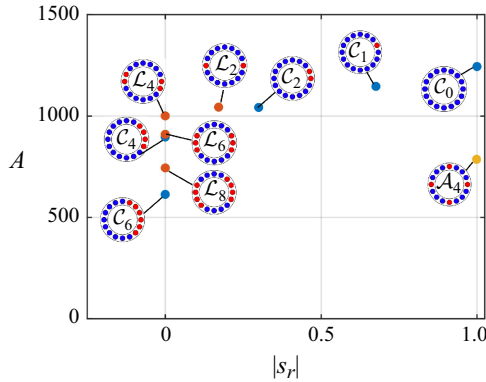


Figure 12. Unstable configurations in the (A, s_r) plane.

It is worth remembering that the nature angle χ , that is used in many recent studies of azimuthal instabilities (see for instance Ghirardo & Bothien 2018; Faure-Beaulieu & Noiray 2020; Indlekofer *et al.* 2022), is linked to the spin ratio by $\chi = \tan^{-1} s_r$.

Now, s_r may be expressed in terms of the amplitudes A_1 and A_2 of the eigenmodes ψ_1 and ψ_2 using relations derived in Appendix D. One gets

$$s_r = \frac{A_1 A_2 \sin(\varphi_1 - \varphi_2) \cos 2\theta_0}{A_1^2 \cos^2 \theta_0 - A_2^2 \sin^2 \theta_0}, \quad (5.28)$$

where θ_0 is the anti-nodal line position, which is also expressed in terms of A_1 and A_2 in Appendix D.

Statistics for the experimental nodal line position, spin ratio time series and joint probability density functions for A_+ and A_- can be found in Latour *et al.* (2024a). The nature of the mode at limit cycle is here represented by placing the limit-cycle characteristics of the unstable configurations, obtained from the resolution of the ODEs, in the $(|s_r|, A)$ plane, as shown in figure 12. In cases C_0 and A_4 , one finds $|s_r| = 1$, corresponding to a purely spinning mode. While calculations for symmetric unstable configurations lead to a spinning mode, experiments indicate that the spin ratio continuously changes between -1 and +1. This difference in behaviour between calculations and experiments confirms findings by Noiray *et al.* (2011) and Faure-Beaulieu & Noiray (2020) and is due, according to these authors, to the absence of a stochastic forcing. Such a forcing, which idealizes the effect of turbulence, is needed to obtain a variable spin ratio taking values over the interval $[-1, +1]$.

It is also concluded from figure 12 that:

- (i) Weak asymmetry in the staging pattern leads to a mixed mode (C_1, C_2 and L_2).
- (ii) Strong asymmetry in the staging pattern gives rise to a standing mode (C_4, C_6, L_4, L_6 and L_8), with the nodal line aligned with the S-injectors median diameter. When standing modes prevail, the nodal line position predicted analytically corresponds to that observed experimentally.

5.6. Sensitivity analysis

It is natural at this stage to examine the sensitivity of the limit-cycle amplitudes to the choice of the FDF gain formulation and fitting coefficients. This is done here for the linear and quadratic fits shown in figure 13 for injectors U and S. The linear fit used in § 5.4 is

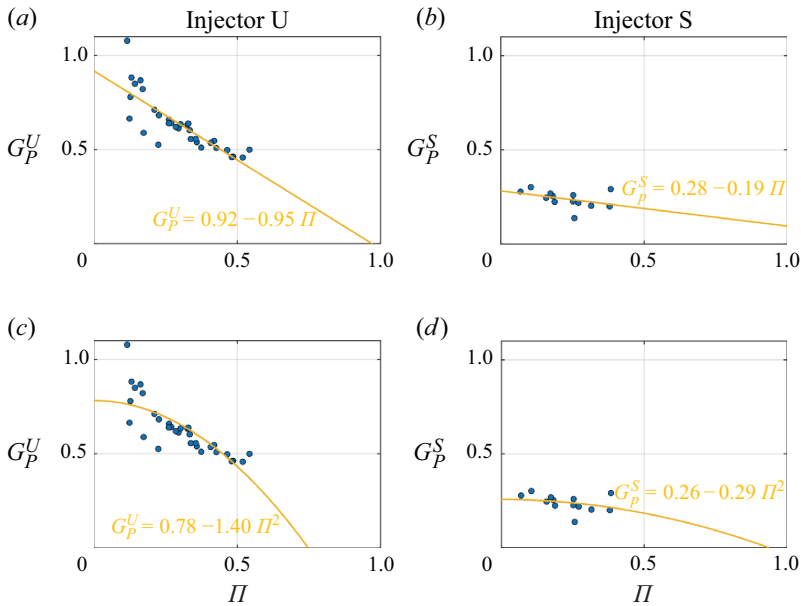


Figure 13. Linear (a,b) and quadratic (c,d) fits for the pressure-based FDF gain experimental data for injector U (a,c) and injector S (b,d).

first compared with a quadratic FDF gain formulation of the form $G_p = \beta - \kappa \Pi^2$. The predicted limit-cycle amplitudes are shown for the linear and quadratic expressions in figure 14(a) for type C configurations. One can see that both formulations lead to similar trends and oscillation amplitude values.

The sensitivity of the calculated amplitudes to the regression coefficients is then tested by changing by $\pm 5\%$ the fitted β and κ values for injector U. Results of this analysis are plotted in figure 14(b,c) for the linear fit, for type C configurations. One can see that the calculated results are most sensitive to β as a $\pm 5\%$ change in the value of this parameter induces a ± 200 Pa variation in the limit-cycle amplitude. A $\pm 5\%$ change in κ has a lesser impact on the predicted limit-cycle oscillation amplitudes. A similar sensitivity analysis for the quadratic fit, not reproduced here, leads to the same conclusions.

6. Determination of growth rate and comparison with that deduced from an acoustic energy balance

The dynamical equations for the slow-flow variables describe the evolution of the system as a function of time. It is interesting to ask whether these equations can be used to derive an expression for the instantaneous growth rate and, in a second stage, compare this expression with that obtained by Latour *et al.* (2024a) by making use of energy balance principles. As we will see, this comparison is not straightforward because one has to link the slow variables A_1 and A_2 , corresponding to the amplitudes of the two perpendicular standing modes ψ_1 and ψ_2 , to the amplitudes A_+ and A_- , associated with the azimuthal waves propagating in the CCW and CW directions. This requires some algebra but allows a term by term comparison between expressions obtained in two notably different ways.

We specifically consider the evolution of $A_1^2 + A_2^2$ and wish to deduce the effective growth rate, defined as $\omega'_i = \omega_i - \alpha/2$, from the logarithmic derivative of this quantity

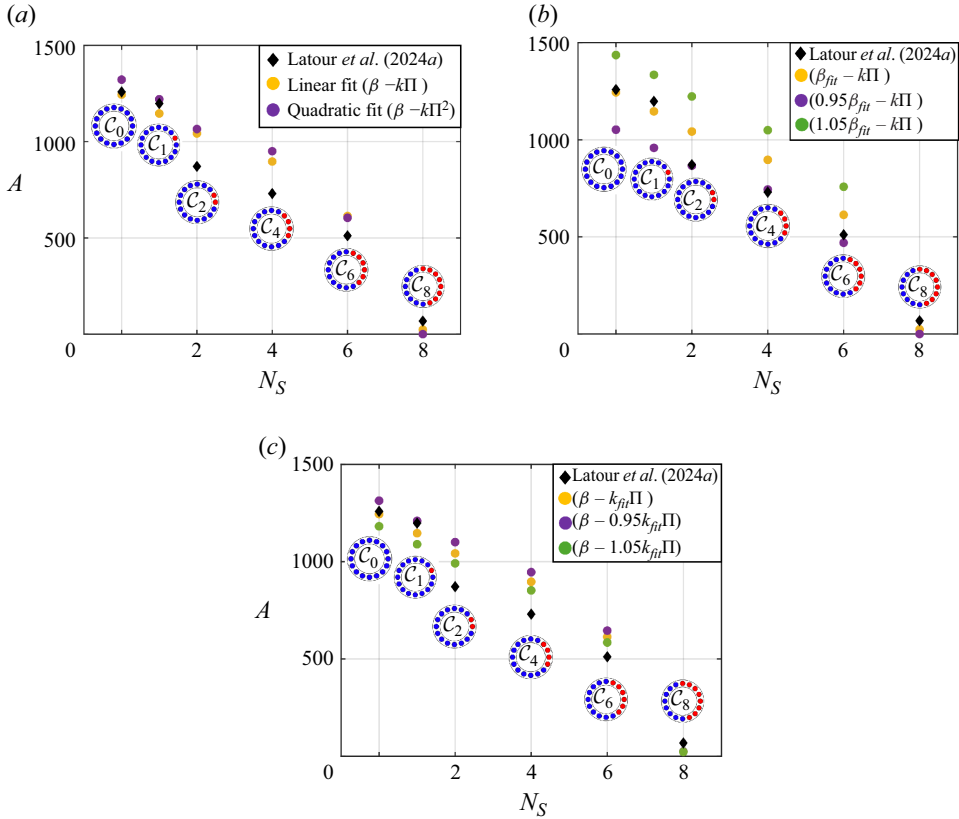


Figure 14. Comparison between a linear and a quadratic expression for the FDF gain on the limit-cycle oscillation amplitude (a). Effects of a $\pm 5\%$ change in the β (b) and κ (c) coefficients values on the analytical limit-cycle oscillation amplitudes for type \mathcal{C} configurations. Here N_S corresponds to the number of S-injectors.

$$\omega'_i = \frac{1}{2} \frac{1}{(A_1^2 + A_2^2)} \frac{d}{dt} (A_1^2 + A_2^2). \quad (6.1)$$

Multiplying the first two equations in the system 5.24 by A_1 and A_2 , respectively, one obtains

$$\begin{aligned} \frac{1}{2} \frac{dA_1^2}{dt} &= -\frac{\alpha}{2} A_1^2 + \frac{\gamma - 1}{2\Lambda} \sum_{j=1}^N \frac{\dot{Q}_0}{\rho U_b^2} G_{p_j} [A_1^2 \cos \varphi_{p_j} \cos^2 \theta_j \\ &\quad + A_2 A_1 \cos(\varphi_{p_j} + \varphi_{12}) \sin \theta_j \cos \theta_j] \\ \frac{1}{2} \frac{dA_2^2}{dt} &= -\frac{\alpha}{2} A_2^2 + \frac{\gamma - 1}{2\Lambda} \sum_{j=1}^N \frac{\dot{Q}_0}{\rho U_b^2} G_{p_j} [A_2^2 \cos \varphi_{p_j} \sin^2 \theta_j \\ &\quad + A_1 A_2 \cos(\varphi_{p_j} + \varphi_{21}) \sin \theta_j \cos \theta_j], \end{aligned} \quad (6.2)$$

where $\varphi_{12} = \varphi_1 - \varphi_2 = -\varphi_{21}$. These two equations may be summed and the result, when divided by $A_1^2 + A_2^2$, yields an expression of the effective growth rate. Assuming that $\dot{Q}_0/(\rho U_b^2)$ is the same for all injectors, one finally obtains

$$\omega'_i = -\frac{\alpha}{2} + \frac{\gamma - 1}{2\Lambda} \frac{\dot{Q}_0}{\rho U_b^2} \sum_{j=1}^N G_{pj} \cos \varphi_{pj} \left[\frac{1}{2} + \frac{1}{2} \frac{A_1^2 - A_2^2}{A_1^2 + A_2^2} \cos 2\theta_j + \frac{A_1 A_2}{A_1^2 + A_2^2} \sin 2\theta_j \cos(\varphi_1 - \varphi_2) \right]. \quad (6.3)$$

This expression may be used to determine the effective growth rate as a function of the two amplitudes A_1 and A_2 and of the phase difference $\varphi_1 - \varphi_2$. It is interesting, at this point, to start from (6.3) and obtain a formulation in terms of the wave amplitudes, A_+ and A_- , and phase angles, ϕ_+ and ϕ_- . This can be done by making use of the following relations, derived in Appendix D:

$$A_1^2 + A_2^2 = 2(A_+^2 + A_-^2), \quad (6.4)$$

$$A_1^2 - A_2^2 = 4A_+A_- \cos(\phi_- - \phi_+), \quad (6.5)$$

$$A_1 A_2 \cos(\varphi_1 - \varphi_2) = 2A_+A_- \sin(\phi_- - \phi_+). \quad (6.6)$$

It is also worth noting that $\phi_- - \phi_+ = 2\theta_0$, where θ_0 designates the anti-nodal line location. Inserting the previous expressions in (6.3), one finds, after some algebra, that

$$\omega'_i = -\frac{\alpha}{2} + \frac{\gamma - 1}{4\Lambda} \frac{\dot{Q}_0}{\rho U_b^2} \sum_{j=1}^N G_{pj} \cos \varphi_{pj} \left[1 + \frac{2A_+A_-}{A_+^2 + A_-^2} \cos 2(\theta_j - \theta_0) \right]. \quad (6.7)$$

One may then isolate the growth rate ω_i and insert $\Lambda = (1/4)V$ so that

$$\omega_i = (\gamma - 1) \frac{\dot{Q}_0}{\rho U_b^2 V} \sum_{j=1}^N G_{pj} \cos \varphi_{pj} \left[1 + \frac{2A_+A_-}{A_+^2 + A_-^2} \cos 2(\theta_j - \theta_0) \right]. \quad (6.8)$$

One may now use the relations between the FDFs $\mathcal{F}_p = G_p \exp(i\varphi_p)$ and $\mathcal{F}_v = G_F \exp(i\varphi_F)$ gains and phases

$$G_p = \frac{1}{\gamma} \frac{G_F}{M G_\zeta} \frac{\rho U_b^2}{p_0}, \quad (6.9)$$

$$\varphi_p = \varphi_F - \varphi_\zeta, \quad (6.10)$$

where G_ζ and φ_ζ represent the modulus and phase of the effective impedance at the flame, which is discussed in Appendix A. Inserting these relations in the growth rate expression (6.8) and using the notations of Latour *et al.* (2024a), $A_+ = |a|$, $A_- = |b|$, one obtains

$$\omega_i = \frac{(\gamma - 1)}{\gamma} \frac{\dot{Q}_0}{p_0 V} \psi_f^2 \sum_{j=1}^N \frac{G_{Fj}}{M G_\zeta} \cos(\varphi_{Fj} - \varphi_{\zeta j}) \left[1 + \frac{2|a||b|}{|a|^2 + |b|^2} \cos 2(\theta_j - \theta_0) \right], \quad (6.11)$$

which exactly matches that derived in Latour *et al.* (2024a) (expression 4.29 of that reference). It is worth underlining that this growth rate expression has been obtained in the same form by making use of two notably different methods: that formulated previously is based on acoustic energy principles, while that derived in the present article relies on dynamical equations deduced from the wave equation. This is synthesized graphically in figure 15. This match strengthens the analysis by Latour *et al.* (2024a) and serves as a further validation of the present calculations.

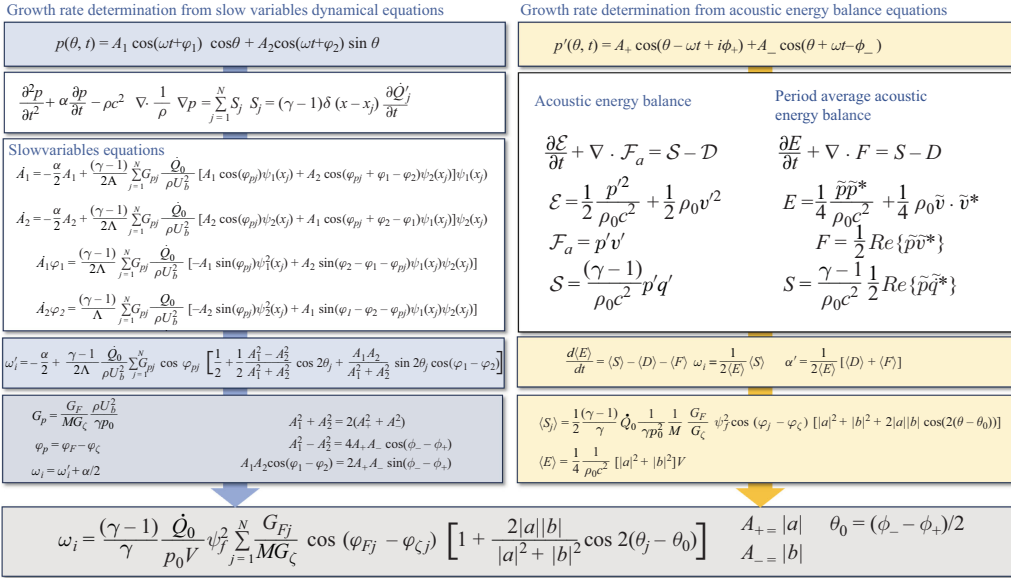


Figure 15. Comparison of two approaches for growth rate determination: slow-flow variable dynamical equations and acoustic energy balance equations.

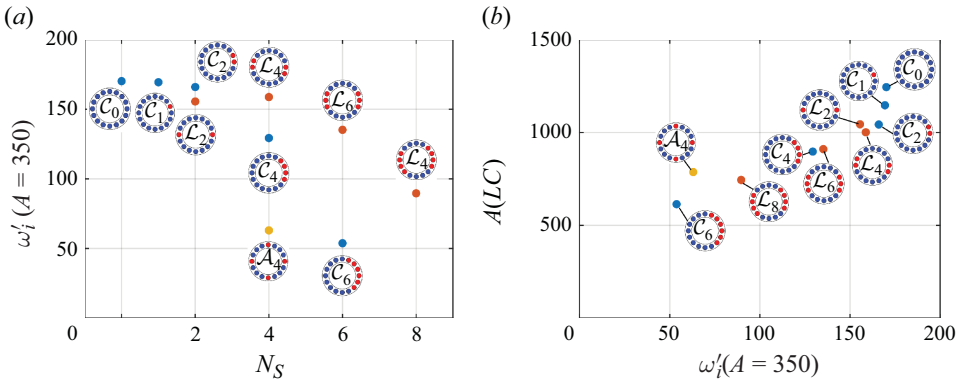


Figure 16. Effective growth rate ω'_i as a function of the number N_S of S-injectors (a) and limit-cycle amplitude $A(LC)$ as a function of the effective growth rate (b).

The growth rate may now be calculated for an oscillation level $A = 350$ Pa (corresponding to the level of fluctuation used for FDF measurements in an externally modulated single-injector configuration in Latour *et al.* (2024a)) using (6.8) and the result is plotted, as a function of the number of S-injectors N_S for the different configurations investigated, in figure 16(a). The trends found match those calculated in Latour *et al.* (2024a) using a growth rate expression derived from acoustic energy balance equations, and FDF data measured in the weakly nonlinear regime as an input. It is also instructive to plot the limit-cycle oscillation amplitude, $A(LC)$, as a function of the effective growth rate, ω'_i , calculated in the linear range (for a low level of oscillation). The corresponding results are shown in figure 16(b). One finds that, the higher the effective growth rate (in the linear range), the higher the limit-cycle oscillation amplitude, a feature that is

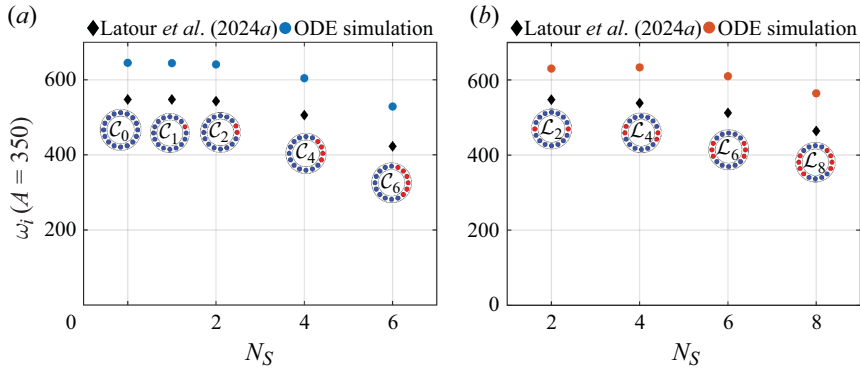


Figure 17. Comparison between growth rates determined from velocity-based FDF data in Latour *et al.* (2024a) (diamonds) and growth rates deduced from the slow-flow equations in the linear range (circles) for type \mathcal{C} (a) and type \mathcal{L} (b) configurations.

already present in Latour *et al.* (2024a) (figure 16b of that reference). A quantitative comparison between the growth rates calculated from FDF data in Latour *et al.* (2024a) and the growth rates calculated for a relatively low amplitude level from the slow-flow equations using (6.8) is also provided in figure 17. The growth rates obtained from ODE simulations are higher than those calculated from FDF data, hinting a slight over-prediction of the source term in the weakly nonlinear range with the linear modelling adopted for the HRR.

A further examination of the link between the linear growth rate and the amplitude of oscillation at limit cycle is proposed in Appendix E, where an analytical expression is derived by assuming that the coupling involves a standing mode. It is shown that this expression provides limit-cycle amplitudes that follow the trends observed experimentally and yields reasonable estimates of the measured amplitudes.

7. Conclusion

The analysis carried out in this article combines a new technique for controlling the limit-cycle oscillation level in an annular combustor with a theoretical representation of the system’s combustion dynamics in terms of slow-flow variables. This is used to explore the evolution toward the limit cycle, calculate growth rates, determine the level of oscillation and the nature of the coupling mode at limit cycle. It is first shown that pressure-based FDFs may be obtained from well-controlled experiments in an annular combustor by simultaneously recording the pressure and HRR signals under self-sustained oscillations. This is done by controlling the nature of the mode and the limit-cycle oscillation amplitude by mixing two types of injection units leading to different flame dynamics. In particular, the collected experimental data can be used to describe the saturation in the flame response with increasing pressure amplitude levels and obtain an experimentally valid representation of the gain and phase evolution as a function of amplitude. On that basis, it is possible to revisit the theoretical modelling of the flame response to acoustic disturbances and replace current models based on a third-order polynomial description of the HRR fluctuations as a function of the pressure oscillation. In the new model proposed in this work, the flame response, described in terms of HRR fluctuations, appears as a linearly decreasing function of the pressure amplitude level. A generic instability analysis framework is used in a first stage to show that this provides an improved representation of the saturation leading to the limit cycle. This model is used in a second stage as an input in

the equations governing the dynamics of an annular combustor as it evolves to a limit cycle. The theoretically predicted limit-cycle oscillation amplitudes using SFVE are compared with experimental data collected in a set of staging experiments carried out in a multiple injector annular combustor MICCA. The model is shown to qualitatively reproduce and quantitatively retrieve experimental observations, in terms of limit-cycle amplitude levels and nature of the modes. There are, admittedly, some differences between calculations and experiments but the general agreement is quite satisfactory. Finally, an expression of the growth rate is extracted from the SFVE, and compared with another expression of that quantity obtained previously by starting from acoustic energy balance principles. The two expressions are found to exactly match, leading to identical growth rate values. It is also demonstrated, perhaps for the first time, that it is possible to predict limit-cycle amplitude levels of instabilities coupled by an azimuthal mode in an annular combustor. This work hence provides a unified framework, bridging results obtained with FDF data obtained in single-injector experiments in the weakly nonlinear range, and flame response modelling, derived from pressure-based FDF measurements under controlled limit-cycle self-sustained oscillations.

Supplementary material. The supplementary material for this article can be found at <https://doi.org/10.1017/jfm.2025.10>.

Funding. This work is partially supported as part of the France 2030 programme ANR-22-CE05-0022-02 FlySAFe project.

Declaration of interests. The authors report no conflict of interest.

Appendix A. Link between the FDFs based on relative velocity fluctuation and on pressure

The standard FDF uses as input variable the relative velocity fluctuation v'/\bar{v} and may be defined by

$$\mathcal{F}_v = \frac{\dot{Q}'/\dot{Q}_0}{v'/\bar{v}}. \quad (\text{A1})$$

In this article we use an FDF based on pressure defined by

$$\mathcal{F}_p = \frac{\dot{Q}'/\dot{Q}_0}{p'/(ρU_b^2)}. \quad (\text{A2})$$

The velocity and pressure fluctuations acting on the flame may be linked by an effective impedance ζ defined by

$$\zeta = p'/(ρcv'). \quad (\text{A3})$$

Using the previous three expressions one finds that

$$\mathcal{F}_v = \mathcal{F}_p \zeta M \frac{\gamma p_0}{\rho U_b^2}, \quad (\text{A4})$$

where $M = \bar{v}/c$ is the Mach number at the flame and where $\gamma p_0 = \rho c^2$. It is convenient to introduce the gains and phases of the FDFs and of the effective impedance $\mathcal{F}_v = G_F e^{i\varphi_F}$, $\mathcal{F}_p = G_p e^{i\varphi_p}$, $\zeta = G_\zeta e^{i\varphi_\zeta}$ and deduce

$$G_p = \frac{G_F}{M G_\zeta} \frac{\rho U_b^2}{\gamma p_0} \quad (\text{A5})$$

and

$$\varphi_p = \varphi_F - \varphi_\zeta. \tag{A6}$$

As pointed out by a reviewer, the impedance used in this derivation is not purely acoustic, and contains effects, such as shedding and convection of vortical structures. This results from the method used to determine the FDF \mathcal{F}_v , which is obtained in Latour *et al.* (2024a) by using velocity fluctuations measured with laser Doppler anemometry (LDA), which does not distinguish purely acoustic velocity fluctuations and velocity disturbances of a different type. The impedance ζ simply serves to link \mathcal{F}_v and \mathcal{F}_p .

Appendix B. Justification of the assumption $g'(a)a/\omega_0 \ll 1$

The easiest way to determine the order of magnitude of $g'(a)a/\omega_0$ is to start with the amplitude equation corresponding to a linearly decreasing function $g(a)$

$$\frac{1}{a} \frac{da}{dt} = \frac{1}{2}(g(a) - \alpha). \tag{B1}$$

One immediately identifies the rate of change of the amplitude on the left-hand side. This is the effective growth rate $\omega'_i(a)$. When the amplitude is very small the effective growth rate is $\omega'_i(0) = (1/2)(g(0) - \alpha)$ and this expression appears on the right-hand side. Now, $|g(a) - g(0)| \geq \max[g'(a)a]$, and dividing the previous equation by ω_0 , one obtains

$$\left| \frac{\omega'_i(a) - \omega'_i(0)}{\omega_0} \right| \geq \frac{1}{2} \max \left[\frac{g'(a)a}{\omega_0} \right]. \tag{B2}$$

Thus

$$\max \left[\left| \frac{g'(a)a}{\omega_0} \right| \right] \leq 2 \frac{|\Delta\omega'_i|}{\omega_0} \leq 2 \frac{|\omega'_i(0)|}{\omega_0}. \tag{B3}$$

The linear growth rate is typically small compared with the angular frequency of oscillation. In the present experiments $\omega'_i(0) \simeq 100 \text{ s}^{-1}$ while $\omega_0 \simeq 2\pi(800) = 5000 \text{ rad s}^{-1}$ so that

$$\max \left[\left| \frac{g'(a)a}{\omega_0} \right| \right] < 0.04. \tag{B4}$$

The approximate expression of $1/\Delta$ is clearly acceptable.

Appendix C. Normal mode expansion of the pressure field

The derivation of the slow-flow equations relies on an expansion of the pressure field on the set of normal modes of the combustor. The objective of this appendix is to specify the modal eigenfunctions that pertain to the annular geometry of the MICCA combustor, discuss their indexing, determine the value of the normalization constant and briefly explain the method of projection that yields the set of dynamical equations (5.5).

One assumes in what follows that the combustor is annular and that the distance between the lateral walls enclosing the chamber is small compared with the mean radius of the system. In this situation there is no dependence on the radial coordinate and one only needs to consider the axial and azimuthal coordinates x and θ . One also assumes that the backplane is rigid like the two sidewalls and that the exhaust is open to the atmosphere.

Assuming a constant value for the speed of sound, solutions of the wave equation

$$\rho c^2 \nabla \cdot \frac{1}{\rho} \nabla \Psi_{mn} + \omega_{mn}^2 \Psi_{mn} = 0, \tag{C1}$$

for the previous boundary conditions may be cast in the form

$$\Psi_{mn}^{(1)}(x, \theta) = \psi_m^{\parallel}(x) \cos(n\theta), \tag{C2}$$

$$\Psi_{mn}^{(2)}(x, \theta) = \psi_m^{\parallel}(x) \sin(n\theta). \tag{C3}$$

In these expressions $\psi_m^{\parallel}(x)$ represent the axial wave function of order m , $\psi_m^{\parallel}(x) = \cos[m\pi x/(2l)]$ while $\cos(n\theta)$ and $\sin(n\theta)$ designate the azimuthal wave functions of order n . For a given eigenvalue ω_{mn} , there are two independent modes in the azimuthal direction that correspond to the cosine and sine functions. It is convenient to use an index $\nu = 1$, or 2 to distinguish these two functions. The pressure field may be expanded over this double set of normal modes

$$p(x, \theta, t) = \sum_{mn} \eta_{mn}^{(1)}(t) \Psi_{mn}^{(1)} + \sum_{mn} \eta_{mn}^{(2)}(t) \Psi_{mn}^{(2)}. \tag{C4}$$

It is a simple matter to show that the normal modes $\Psi_{mn}^{(\nu)}$ form an orthogonal basis and to determine the normalization constant

$$\Lambda_{mn}^{\nu} = \int_V [\Psi_{mn}^{(\nu)}]^2 dV. \tag{C5}$$

For modes that have an azimuthal number n that is non-zero, one finds that $\Lambda_{mn}^{\nu} = (1/4)V$ and this common value will be designated by Λ . Purely axial modes ($n = 0$) feature a normalization constant $\Lambda_{m0} = (1/2)V$ but these modes are not considered in the present analysis. The pressure field expansion may be introduced in the wave equation (5.1) which is then projected on the mode $\Psi_{mn}^{(\nu)}$. This yields

$$\ddot{\eta}_{mn}^{\nu} + \alpha \dot{\eta}_{mn}^{\nu} + \omega_{mn}^2 \eta_{mn}^{\nu} = \frac{1}{\Lambda_{mn}^{\nu}} \int_V S \Psi_{mn}^{\nu} dV \text{ for } \nu = 1, 2. \tag{C6}$$

The dynamical equations are here derived by considering the 1A1L mode, i.e. the first azimuthal $n = 1$, first longitudinal $m = 1$ mode. In the analysis we also assume that the flames act like point sources located at an axial distance x_f from the backplane and at azimuthal angles θ_j , $j = 1, \dots, N$ so that the axial eigenfunction is evaluated at that distance. It is then convenient to set $\psi_f = \psi_1^{\parallel}(x_f)$ and write the pressure field acting on the flames in the form

$$p(x_f, \theta, t) = \psi_f [\eta_{11}^{(1)}(t) \cos \theta + \eta_{11}^{(2)}(t) \sin \theta]. \tag{C7}$$

The notation can be simplified by replacing the previous expression by

$$p(x_f, \theta, t) = \psi_f [\eta_1(t) \cos \theta + \eta_2(t) \sin \theta]. \tag{C8}$$

The two modal amplitudes then satisfy the set of differential equations (5.5).

Appendix D. Relation between the standing modes amplitudes A_1 and A_2 and the azimuthal wave amplitudes A_+ and A_-

It is useful to establish links between the present representation of the pressure field

$$p'(\theta, t) = A_1 \cos(\omega t + \varphi_1) \cos \theta + A_2 \cos((\omega t + \varphi_2) \sin \theta \tag{D1}$$

and the standard formulation of this field in the form of a sum of two azimuthal waves

$$p'(\theta, t) = \text{Re}\{A_+ \exp(i\theta - i\omega t + i\phi_+) + A_- \exp(-i\theta - i\omega t + i\phi_-)\} \quad (\text{D2})$$

$$= A_+ \cos(\theta - \omega t + \phi_+) + A_- \cos(\theta + \omega t - \phi_-). \quad (\text{D3})$$

By matching these two representations one finds that

$$A_+ \cos(\omega t - \phi_+) + A_- \cos(\omega t - \phi_-) = A_1 \cos(\omega t + \varphi_1), \quad (\text{D4})$$

$$A_+ \sin(\omega t - \phi_+) - A_- \sin(\omega t - \phi_-) = A_2 \cos(\omega t + \varphi_2). \quad (\text{D5})$$

One may then deduce a complex versions of these two expressions

$$A_+ e^{i\phi_+} + A_- e^{i\phi_-} = A_1 e^{-i\varphi_1}, \quad (\text{D6})$$

$$A_+ e^{i\phi_+ + i\pi/2} - A_- e^{i\phi_- + i\pi/2} = A_2 e^{-i\varphi_2}. \quad (\text{D7})$$

Multiplying these two expressions by their complex conjugates, and multiplying the first by the complex conjugate of the second one obtains

$$A_1^2 = A_+^2 + A_-^2 + 2A_+A_- \cos(\phi_- - \phi_+), \quad (\text{D8})$$

$$A_2^2 = A_+^2 + A_-^2 - 2A_+A_- \cos(\phi_- - \phi_+), \quad (\text{D9})$$

$$A_1A_2 \cos(\varphi_1 - \varphi_2) = 2A_+A_- \sin(\phi_- - \phi_+). \quad (\text{D10})$$

It is then easy to deduce the following set of expressions:

$$A_1^2 + A_2^2 = 2(A_+^2 + A_-^2), \quad (\text{D11})$$

$$A_1^2 - A_2^2 = 4A_+A_- \cos(\phi_- - \phi_+), \quad (\text{D12})$$

$$A_1A_2 \cos(\varphi_1 - \varphi_2) = 2A_+A_- \sin(\phi_- - \phi_+), \quad (\text{D13})$$

$$A_1A_2 \sin(\varphi_1 - \varphi_2) = A_+^2 - A_-^2. \quad (\text{D14})$$

These expressions can then be used to write the growth rate ω_i in terms of the azimuthal wave amplitudes A_+ , A_- and phases ϕ_+ , ϕ_- (see § 5). It is also a simple matter to link $\varphi_1 - \varphi_2$ and θ_0 . Some calculations yield

$$\tan(2\theta_0) = \frac{2A_1A_2}{A_1^2 - A_2^2} \cos(\varphi_1 - \varphi_2). \quad (\text{D15})$$

Nevertheless, care has to be taken to ensure that the correct value of θ_0 is obtained.

Using

$$\sin(2\theta_0) = \frac{2A_1A_2 \cos(\varphi_1 - \varphi_2)}{[(A_1^2 + A_2^2)^2 - 4A_1^2A_2^2 \sin^2(\varphi_1 - \varphi_2)]^{1/2}} \quad (\text{D16})$$

and

$$\cos(2\theta_0) = \frac{A_1^2 - A_2^2}{[(A_1^2 + A_2^2)^2 - 4A_1^2A_2^2 \sin^2(\varphi_1 - \varphi_2)]^{1/2}}, \quad (\text{D17})$$

one gets the following expression, ensuring that θ_0 is always defined in the $[-\pi/2, \pi/2]$ range:

$$\theta_0 = \frac{1}{2} \text{sign}\{\sin 2\theta_0\} \cos^{-1}[\cos 2\theta_0]. \quad (\text{D18})$$

It is also interesting to express the spin ratio as a function of the amplitudes A_1, A_2 and phases φ_1, φ_2 . The spin ratio is defined by $s_r = (A_+ - A_-)/(A_+ + A_-)$ which may also be written as $s_r = (A_+^2 - A_-^2)/(A_+^2 + A_-^2 + 2A_+A_-)$. Using expressions (D11) to (D14) one may write

$$s_r = \frac{A_1 A_2 \sin(\varphi_1 - \varphi_2)}{(1/2)(A_1^2 + A_2^2) + (1/2)(A_1^2 - A_2^2)/\cos 2\theta_0}, \tag{D19}$$

which becomes after some algebra

$$s_r = \frac{A_1 A_2 \sin(\varphi_1 - \varphi_2) \cos 2\theta_0}{(A_1^2 \cos^2 \theta_0 - A_2^2 \sin^2 \theta_0)}. \tag{D20}$$

Appendix E. Analytical expression of the limit-cycle oscillation amplitude

An analytical expression of the limit-cycle amplitude may be derived from the general expression of the growth rate by making use of some simplifying assumptions. In what follows we consider two families of injectors designated by U and S and assume that the gain of the pressure based describing function is a linear function of the reduced r.m.s. pressure $\Pi_j = (p'_j)_{rms}/\rho U_b^2$ so that one can write

$$G_{p_j}^U = \beta^U - \kappa^U \Pi_j, \tag{E1}$$

$$G_{p_j}^S = \beta^S - \kappa^S \Pi_j. \tag{E2}$$

It is also assumed, for the sake of simplicity, that the phases of the pressure based describing function do not change with the amplitude Π_j so that one may use constant values for the phases $\varphi_j^U = \varphi^U$ and $\varphi_j^S = \varphi^S$. The present calculations are carried out by assuming that the coupling is induced by a standing mode. This is the case for example in configurations $\mathcal{C}_4, \mathcal{C}_6$ and $\mathcal{L}_2, \mathcal{L}_4, \mathcal{L}_6, \mathcal{L}_8$. The growth rate may then be written in the form

$$\omega_i = \frac{1}{\Lambda}(\gamma - 1) \frac{\psi_f^2}{2} \frac{\dot{Q}_0}{\rho U_b^2} \left\{ \cos \varphi_p^U \sum_{j=1}^{N_u} \cos^2 \theta_j (\beta^U - \kappa^U \Pi_j) + \cos \varphi_p^S \sum_{j=1}^{N_s} \cos^2 \theta_j (\beta^S - \kappa^S \Pi_j) \right\}. \tag{E3}$$

It is possible to identify in this expression the linear growth rate corresponding to low amplitude levels $\omega_i(0)$ and another term χ that defines the change in ω_i due to the growth of oscillation amplitude. One may thus write

$$\omega_i = \omega_i(0) - \chi, \tag{E4}$$

where

$$\omega_i(0) = \omega_i^U(0) \left\{ 1 - \frac{\beta^U \cos \varphi_p^U - \beta^S \cos \varphi_p^S}{\beta^U \cos \varphi_p^U} \frac{2}{N} \sum_{j=1}^{N_s} \cos^2 \theta_j \right\}, \tag{E5}$$

$$\chi = \omega_i^U(0) \frac{\kappa^U}{\beta^U} \left\{ \frac{8}{3\pi} - \frac{\kappa^U \cos \varphi_p^U - \kappa^S \cos \varphi_p^S}{\kappa^U \cos \varphi_p^U} \frac{2}{N} \sum_{j=1}^{N_s} \cos^2 \theta_j |\cos \theta_j| \right\} \Pi_{max}, \tag{E6}$$

Configuration	\mathcal{C}_4	\mathcal{C}_6	\mathcal{L}_2	\mathcal{L}_4	\mathcal{L}_6	\mathcal{L}_8
Experimental amplitude A (Pa)	730	510	1127	1418	1225	1120
Theoretical amplitude $a/2^{1/2}$ (Pa)	913	640	1050	1014	926	765

Table 3. Comparison between the experimental limit-cycle amplitudes, A , and the values estimated from the analytical model.

where

$$\omega_i^U(0) = (\gamma - 1)\psi_f^2 \frac{\dot{Q}_0 N}{\rho U_b^2 V} \cos \varphi_p^U \beta^U \tag{E7}$$

designates the linear growth rate when all injectors are of the U-type, and

$$\Pi_{max} = \frac{a}{2^{1/2}} \frac{1}{\rho U_b^2} \psi_f \tag{E8}$$

represents the maximum value of the reduced r.m.s. pressure level. It is convenient to define a parameter C such that

$$C = \left\{ \frac{8}{3\pi} - \frac{\kappa^U \cos \varphi_p^U - \kappa^S \cos \varphi_p^S}{\kappa^U \cos \varphi_p^U} \frac{2}{N} \sum_{j=1}^{N_s} \cos^2 \theta_j |\cos \theta_j| \right\}. \tag{E9}$$

With these definitions one may now express the growth rate in the following form:

$$\omega_i = \omega_i(0) - \omega_i^U(0) C \Pi_{max}. \tag{E10}$$

When all injectors are of the U-type, $C = 8/(3\pi)$. When the number N_s is small and all S injectors are located near the pressure nodal line $C \simeq 8/(3\pi)$ and one may also use that expression. In the more general case, one has to calculate C .

It is now easy to determine the value of Π_{max} at the limit cycle. This can be done by noting that at the limit cycle $\omega_i = \alpha$ so that

$$\Pi_{max}(lc) = \frac{\omega_i(0) - \alpha}{C(\kappa^U/\beta^U)\omega_i^U(0)}. \tag{E11}$$

One obtains

$$\frac{a}{2^{1/2}} = \frac{\beta^U}{\kappa^U} \frac{\omega_i(0) - \alpha}{C\omega_i^U(0)\psi_f} \rho U_b^2. \tag{E12}$$

The previous expressions feature a linear dependence of the limit-cycle amplitude with respect to the effective growth rate ω'_i . They can be used to predict the r.m.s. pressure level at the limit cycle $a/2^{1/2}$ and compare this value with A determined experimentally. Table 3 gathers predicted values and experimental data for the injector arrangements corresponding to a coupling by a standing mode. One can see that the trends (lower amplitude values for type \mathcal{C} than type \mathcal{L} configurations) are correctly retrieved. A good match is observed between the model's predictions and the experimental data, and, as for the limit-cycle amplitudes obtained by solving the slow-flow variables ODEs (see § 5), larger discrepancies are observed between experimental data and model prediction for type \mathcal{L} than for type \mathcal{C} configurations.

- ALHAFFAR, A., LATOUR, V., PATAT, C., DUROX, D., RENAUD, A., BLAISOT, J.-B., CANDEL, S. & BAILLOT, F. 2024 Comparison of pressure-based flame describing functions measured in an annular combustor under self-sustained oscillations and in an externally modulated linear combustor. *Proc. Combust. Inst.* **40** (1-4), 105249.
- BALACHANDRAN, R., AYOOLA, B.O., KAMINSKI, C.F., DOWLING, A.P. & MASTORAKOS, E. 2005 Experimental investigation of the nonlinear response of turbulent premixed flames to imposed inlet velocity oscillations. *Combust. Flame* **143** (1-2), 37–55.
- BAUERHEIM, M., CAZALENS, M. & POINSOT, T. 2015 A theoretical study of mean azimuthal flow and symmetry effects on thermo-acoustic modes in annular combustors. *Proc. Combust. Inst.* **346**, 271–290.
- BONCIOLINI, G., FAURE-BEAULIEU, A., BOURQUARD, C. & NOIRAY, N. 2021 Low order modelling of thermoacoustic instabilities and intermittency: flame response delay and nonlinearity. *Combust. Flame* **226**, 396–411.
- BOUJO, E., DENISOV, A., SCHUERMANS, B. & NOIRAY, N. 2016 Quantifying acoustic damping using flame chemiluminescence. *J. Fluid Mech.* **808**, 245–257.
- BOURGOUIN, J.-F., DUROX, D., MOECK, J.P., SCHULLER, T. & CANDEL, S. 2013 Self-sustained instabilities in an annular combustor coupled by azimuthal and longitudinal acoustic modes. In *Proceeding of ASME Turbo Expo 2013*, GT2013-95010. ASME.
- COLE, J.D. 1968 *Perturbation Methods in Applied Mathematics*. Blaisdell.
- ĆOSIĆ, B., REICHEL, T. & PASCHEREIT, C. 2012 Acoustic response of a Helmholtz resonator exposed to hot-gas penetration and high amplitude oscillations. *Trans. ASME: J. Engng Gas Turbines Power* **134** (10), 101503.
- CULICK, F. 1994 Some recent results for nonlinear acoustics in combustion chambers. *AIAA J.* **32** (1), 146–169.
- DOWLING, A.P. 1997 Nonlinear self-excited oscillations of a ducted flame. *J. Fluid Mech.* **346**, 271–290.
- DUROX, D., SCHULLER, T., NOIRAY, N., BIRBAUD, A.L. & CANDEL, S. 2009 Rayleigh criterion and acoustic energy balance in unconfined self-sustained oscillating flames. *Combust. Flame* **156** (1), 106–119.
- FAURE-BEAULIEU, A., INDLEKOFER, T., DAWSON, JR. & NOIRAY, N. 2021 Experiments and low-order modelling of intermittent transitions between clockwise and anticlockwise spinning thermoacoustic modes in annular combustors. *Proc. Combust. Inst.* **38** (4), 5943–5951.
- FAURE-BEAULIEU, A. & NOIRAY, N. 2020 Symmetry breaking of azimuthal waves: slow-flow dynamics on the Bloch sphere. *Phys. Rev. Fluids* **5** (2), 023201.
- FAURE-BEAULIEU, A., PEDERGNANA, T. & NOIRAY, N. 2023 Self-sustained azimuthal aeroacoustic modes. Part 2. Effect of swirling mean flow on the modal dynamics. *J. Fluid Mech.* **971**, A22.
- GHIRARDO, G. & BOTHIEN, M.R. 2018 Quaternion structure of azimuthal instabilities. *Phys. Rev. Fluids* **3** (11), 113202.
- GHIRARDO, G., BOUDY, F. & BOTHIEN, M.R. 2018 Amplitude statistics prediction in thermoacoustics. *J. Fluid Mech.* **844**, 216–246.
- GHIRARDO, G., ĆOSIĆ, B., JUNIPER, M.P. & MOECK, J.P. 2015 State-space realization of a describing function. *Nonlinear Dyn.* **82** (1-2), 9–28.
- GHIRARDO, G., JUNIPER, M. & BOTHIEN, M.R. 2018 The effect of the flame phase on thermoacoustic instabilities. *Combust. Flame* **187**, 165–184.
- GHIRARDO, G. & JUNIPER, M.P. 2013 Azimuthal instabilities in annular combustors: standing and spinning modes. *Proc. R. Soc. Lond. A* **469** (2157), 20130232.
- GHIRARDO, G., JUNIPER, M.P. & MOECK, J.P. 2016 Weakly nonlinear analysis of thermoacoustic instabilities in annular combustors. *J. Fluid Mech.* **805**, 52–87.
- GHIRARDO, G., NYGÅRD, H.T., CUQUEL, A. & WORTH, N.A. 2021 Symmetry breaking modelling for azimuthal combustion dynamics. *Proc. Combust. Inst.* **38** (4), 5953–5962.
- HAERINGER, M., MERK, M. & POLIFKE, W. 2019 Inclusion of higher harmonics in the flame describing function for predicting limit-cycles of self-excited combustion instabilities. *Proc. Combust. Inst.* **37** (4), 5255–5262.
- INDLEKOFER, T., FAURE-BEAULIEU, A., DAWSON, JR. & NOIRAY, N. 2022 Spontaneous and explicit symmetry breaking of thermoacoustic eigenmodes in imperfect annular geometries. *J. Fluid Mech.* **944**, A15.
- KASHINATH, K., WAUGH, I. & JUNIPER, M. 2014 Nonlinear self-excited thermoacoustic oscillations of a ducted premixed flame: bifurcations and routes to chaos. *J. Fluid Mech.* **761**, 399–430.
- KRYLOV, N. & BOGOLIUBOV, N. 1950 *Introduction to Nonlinear Mechanics*. Princeton University Press.
- LAERA, D., PRIEUR, K., DUROX, D., SCHULLER, T., CAMPOREALE, S.M. & CANDEL, S. 2017 Impact of heat release distribution on the spinning modes of an annular combustor with multiple matrix burners. *Trans. ASME: J. Engng Gas Turbines Power* **139** (5), 51505.

- LATOUR, V., DUROX, D., RENAUD, A. & CANDEL, S. 2024a Experiments on symmetry breaking of azimuthal combustion instabilities and their analysis combining acoustic energy balance and flame describing functions. *J. Fluid Mech.* **985**, A31.
- LATOUR, V., DUROX, D., RENAUD, A. & CANDEL, S. 2024b Experimental and theoretical estimation of acoustic energy source terms and instability growth rates in an annular combustor. *Proc. Combust. Inst.* **40** (1–4), 105204.
- LIEUWEN, T. 2003 Modeling premixed combustion-acoustic wave interactions: a review. *J. Propul. Power* **19** (5), 765–781.
- MOECK, J., DUROX, D., SCHULLER, T. & CANDEL, S. 2019 Nonlinear thermoacoustic mode synchronization in annular combustors. *Proc. Combust. Inst.* **37** (4), 5343–5350.
- MOECK, J. & PASCHEREIT, O. 2012 Nonlinear interactions of multiple linearly unstable thermoacoustic modes. *Int. J. Spray Combust.* **4** (1), 1–28.
- NAYFEH, A.H. & MOOK, D.T. 1979 *Nonlinear Oscillations*. Wiley.
- NICOUD, F., BENOIT, L., SENSIAU, C. & POINSOT, T. 2007 Acoustic modes in combustors with complex impedances and multidimensional active flames. *AIAA J.* **45** (2), 426–441.
- NOIRAY, N., BOTHIEN, M. & SCHUERMANS, B. 2011 Investigation of azimuthal staging concepts in annular gas turbines. *Combust. Theor. Model.* **15** (5), 585–606.
- NOIRAY, N., DUROX, D., SCHULLER, T. & CANDEL, S. 2008 A unified framework for nonlinear combustion instability analysis based on the flame describing function. *J. Fluid Mech.* **615**, 139–167.
- NOIRAY, N. & SCHUERMANS, B. 2013 On the dynamic nature of azimuthal thermoacoustic modes in annular gas turbine combustion chambers. *Proc. R. Soc. Lond. A* **469** (2151), 20120535.
- NYGÅRD, H.T., GHIRARDO, G. & WORTH, N.A. 2021 Azimuthal flame response and symmetry breaking in a forced annular combustor. *Combust. Flame* **233**, 111565.
- NYGÅRD, H.T., GHIRARDO, G. & WORTH, N.A. 2023 Saturation of flames to multiple inputs at one frequency. *J. Fluid Mech.* **977**, A6.
- NYGÅRD, H.T., MAZUR, M., DAWSON, J.R. & WORTH, N.A. 2019 Flame dynamics of azimuthal forced spinning and standing modes in an annular combustor. *Proc. Combust. Inst.* **37** (4), 5113–5120.
- O'CONNOR, J., ACHARYA, V. & LIEUWEN, T. 2015 Transverse combustion instabilities: acoustic, fluid mechanic, and flame processes. *Prog. Energy Combust. Sci.* **49**, 1–39.
- ORCHINI, A. & JUNIPER, M.P. 2016 Flame double input describing function analysis. *Combust. Flame* **171**, 87–102.
- ORCHINI, A., MENSAH, G. & MOECK, J. 2019 Effects of nonlinear modal interactions on the thermoacoustic stability of annular combustors. *Trans. ASME: J. Engng Gas Turbines Power* **141** (2), 021002.
- ORCHINI, A. & MOECK, J. 2024 Weakly nonlinear analysis of thermoacoustic oscillations in can-annular combustors. *J. Fluid Mech.* **980**, A52.
- PALIÈS, P., DUROX, D., SCHULLER, T. & CANDEL, S. 2011 Nonlinear combustion instability analysis based on the flame describing function applied to turbulent premixed swirling flames. *Combust. Flame* **158** (10), 1980–1991.
- POINSOT, T. 2017 Prediction and control of combustion instabilities in real engines. *Proc. Combust. Inst.* **36** (1), 1–28.
- PRIEUR, K., DUROX, D., SCHULLER, T. & CANDEL, S. 2018 Strong azimuthal combustion instabilities in a spray annular chamber with intermittent partial blow-off. *Trans. ASME: J. Engng Gas Turbines Power* **140** (3), 31503.
- RAJENDRAM SOUNDARARAJAN, P., DUROX, D., RENAUD, A. & CANDEL, S. 2022 Azimuthal instabilities of an annular combustor with different swirling injectors. *Trans. ASME: J. Engng Gas Turbines Power* **144** (11), 111018.
- RAJENDRAM SOUNDARARAJAN, P., DUROX, D., RENAUD, A., VIGNAT, G. & CANDEL, S. 2022 Swirler effects on combustion instabilities analyzed with measured FDFs, injector impedances and damping rates. *Combust. Flame* **238**, 111947.
- SCHULLER, T., MARRAGOU, S., OZTARLIK, G., POINSOT, T. & SELLE, L. 2022 Influence of hydrogen content and injection scheme on the describing function of swirled flames. *Combust. Flame* **240**, 111974.
- SCHULLER, T., POINSOT, T. & CANDEL, S. 2020 Dynamics and control of premixed combustion systems based on flame transfer and describing functions. *J. Fluid Mech.* **894**, P1.
- SCHULLER, T., TRAN, N., NOIRAY, N., DUROX, D., DUCRUIX, S. & CANDEL, S. 2009 The role of nonlinear acoustic boundary conditions in combustion/acoustic coupled instabilities. In *Proceedings of ASME Turbo Expo 2009 GT2009-59390*. ASME.
- SIRIGNANO, W. & KRIEG, J. 2016 Two-time-variable perturbation theory for liquid-rocket combustion instability. *J. Propul. Power* **32** (3), 755–776.

- STOW, S. & DOWLING, A. 2009 A time-domain network model for nonlinear thermoacoustic oscillations. *Trans. ASME: J. Engng Gas Turbines Power* **131** (3), 031502.
- VERHULST, F. 1996 *Nonlinear Differential Equations and Dynamical Systems*. Springer.
- VIGNAT, G. 2020 Injection and combustion dynamics in swirled spray flames and azimuthal coupling in annular combustors. PhD thesis, Université Paris-Saclay, France.
- VIGNAT, G., RAJENDRAM SOUNDARARAJAN, P., DUROX, D., VIÉ, A., RENAUD, A. & CANDEL, S. 2021 A joint experimental and large Eddy simulation characterization of the liquid fuel spray in a swirl injector. *Trans. ASME: J. Engng Gas Turbines Power* **143** (8), 081019.
- WISEMAN, S., GRUBER, A. & DAWSON, J. 2023 Flame transfer functions for turbulent, premixed, ammonia-hydrogen-nitrogen-air flames. *Trans. ASME: J. Engng Gas Turbines Power* **145** (3), 031015.
- WOLF, P., STAFFELBACH, G., GICQUEL, L., MÜLLER, J.-D. & POINSOT, T. 2012 Acoustic and large Eddy simulation studies of azimuthal modes in annular combustion chambers. *Combust. Flame* **159** (11), 3398–3413.
- ZINN, B. & LORES, M. 1972 Application of the Galerkin method in the solution of non-linear axial combustion instability problems in liquid rockets. *Combust. Sci. Technol.* **4**, 269–278.